

FISSION IN EXOTIC NUCLEI USING DENSITY FUNCTIONAL THEORY

By

Zachary Matheson

A DISSERTATION

Submitted to
Michigan State University
in partial fulfillment of the requirements
for the degree of

Physics — Doctor of Philosophy
Computational Mathematics, Science and Engineering — Dual Major

2019

ABSTRACT

FISSION IN EXOTIC NUCLEI USING DENSITY FUNCTIONAL THEORY

By

Zachary Matheson

This is my abstract.

Dedicated to I dunno

ACKNOWLEDGMENTS

I dunno who to acknowledge, either

TABLE OF CONTENTS

| | |
|--|------------|
| LIST OF FIGURES | vii |
| Chapter 1 Introduction | 1 |
| 1.1 History of fission theory | 1 |
| 1.1.1 Liquid drop model | 2 |
| 1.1.2 Strutinsky shell correction approach | 2 |
| 1.1.3 Self-consistent models and the supercomputing era | 3 |
| 1.2 Predicting fission fragments | 4 |
| 1.3 Goals of the project | 5 |
| Chapter 2 Describing Fission Using Nuclear Density Functional Theory | 7 |
| 2.1 Nuclear density functional theory | 8 |
| 2.1.1 Density functional theory | 9 |
| 2.1.1.1 Kinetic energy term | 11 |
| 2.1.1.2 Coulomb interaction term | 11 |
| 2.1.1.3 Nuclear interaction term | 12 |
| 2.1.1.4 Pairing interaction term | 13 |
| 2.1.2 Hartree-Fock-Bogoliubov method | 14 |
| 2.1.2.1 Bogoliubov transformation | 14 |
| 2.1.2.2 HFB equations | 15 |
| 2.1.3 Nucleon localization function | 16 |
| 2.2 Microscopic description of nuclear fission | 17 |
| 2.2.1 Potential energy surfaces | 17 |
| 2.2.2 Collective inertia | 18 |
| 2.2.3 WKB approximation | 19 |
| 2.2.4 Langevin dynamics | 20 |
| Chapter 3 Numerical Implementation | 22 |
| 3.1 Calculating the PES | 22 |
| 3.1.1 PES Tools | 23 |
| 3.2 Calculating the collective inertia | 23 |
| 3.3 Minimum action path | 25 |
| 3.4 Langevin | 26 |
| Chapter 4 Two fission modes in ^{178}Pt | 27 |
| 4.1 Asymmetric fission in the region of ^{180}Hg | 27 |
| 4.2 Multimode fission of ^{178}Pt | 29 |
| 4.3 The physical origin of fragment asymmetry in the neutron-deficient sub-lead region | 31 |

| | | |
|-------------------|---|-----------|
| Chapter 5 | Cluster decay in ^{294}Og | 34 |
| 5.1 | Cluster emission in superheavy elements | 34 |
| 5.2 | Predicted spontaneous fission yields of ^{294}Og | 36 |
| 5.3 | Fragment formation in ^{294}Og | 42 |
| 5.4 | Experimental search for cluster emission in ^{294}Og | 42 |
| Chapter 6 | Fission in the R Process | 45 |
| 6.1 | The role of fission in the astrophysical r process | 45 |
| 6.2 | Fission fragment yields for r-process nuclei | 48 |
| 6.3 | Kilonova and ^{254}Cf | 49 |
| Chapter 7 | Outlook | 51 |
| 7.1 | Perspectives for future model development | 51 |
| 7.1.1 | Numerical challenges | 51 |
| 7.1.2 | Self-consistent stochastic dynamics | 53 |
| 7.2 | Perspectives for future physics applications | 53 |
| 7.2.1 | Half-lives | 53 |
| 7.2.2 | Collective variables | 54 |
| 7.2.3 | Collective inertia in neutron-deficient sublead region | 54 |
| 7.2.4 | Predicting other experimental observables | 54 |
| 7.2.5 | Large-scale calculations with machine learning | 55 |
| 7.3 | Review and conclusions | 57 |
| APPENDICES | | 58 |
| | Appendix A Fragment Identification | 59 |
| A.1 | Fragments and the nucleon localization function | 59 |
| A.2 | The problem of scission | 60 |
| A.3 | Prefragment shell structure | 61 |
| A.4 | Isospin transport | 62 |
| | Appendix B Temperature-Dependent ATDHFB Collective Inertia | 64 |
| B.1 | Fission at finite temperature | 64 |
| B.2 | Finite-temperature density | 65 |
| B.3 | Temperature-dependent ATDHFB | 66 |
| B.3.1 | Review of ATDHFB | 68 |
| B.3.2 | Relation between χ and $\hat{\mathcal{R}}$ | 69 |
| B.3.3 | Kinetic energy at finite temperature | 71 |
| B.3.3.1 | Term proportional to \mathcal{R}_2 | 71 |
| B.3.3.2 | Term proportional to \mathcal{R}_1 | 73 |
| B.3.4 | Collective inertia tensor | 80 |
| B.3.4.1 | The total kinetic energy | 80 |
| B.3.4.2 | Cranking approximation | 82 |
| B.3.4.3 | Collective shape space | 82 |
| B.4 | Numerical implementation | 84 |
| | Appendix C List of My Contributions | 86 |

LIST OF FIGURES

| | | |
|-------------|---|----|
| Figure 3.1: | Collective inertia as a function of finite-difference spacing | 24 |
| Figure 3.2: | Norm of the difference matrix between subsequent iterations of the density | 25 |
| Figure 4.1: | Survey of fragment yields near ^{180}Hg | 28 |
| Figure 4.2: | ^{178}Pt experimental data | 29 |
| Figure 4.3: | UNEDF1-HFB potential energy surface for ^{178}Pt | 30 |
| Figure 4.4: | D1S potential energy surface for ^{178}Pt | 31 |
| Figure 5.1: | Calculated and experimental decay modes for SHE | 35 |
| Figure 5.2: | Dominant decay modes for SHE in a nuclear DFT-based framework. . . | 35 |
| Figure 5.3: | PES comparison for ^{294}Og using EDFs UNEDF1 _{HFB} , D1S, and SkM*. . | 37 |
| Figure 5.4: | N-Z fission fragment yields from ^{294}Og | 40 |
| Figure 5.5: | ^{294}Og heavy fragment masses and charges. | 41 |
| Figure 5.6: | Nucleon localization visualization of ^{294}Og prefragment formation. . . . | 43 |
| Figure 6.1: | Schematic overview of the r process | 46 |
| Figure 6.2: | Final r-process abundances for a neutron star merger scenario with dif- ferent fission fragment distributions. | 47 |
| Figure 6.3: | Isotopes whose fission yields are especially relevant to the r process . . . | 48 |

Chapter 1

Introduction

1.1 History of fission theory

Nuclear fission is the fundamental physical process by which a heavy nucleus decays to two smaller nuclei with comparable masses, and a proper understanding of fission is critical for applications in reactor physics, nuclear astrophysics, and stockpile stewardship. Fission was first observed by Hahn and Straßmann in 1939 [1] as they bombarded uranium atoms with neutrons and detected barium, but the men could not explain their observations at the time. An explanation came shortly thereafter in letters to the editor by Meitner and Frisch [2] and by Bohr [3]. In Meitner and Frisch’s paper they said “On account of their close packing and strong energy exchange, the particles in a heavy nucleus would be expected to move in a collective way which has some resemblance to the movement of a liquid drop. If the movement is made sufficiently violent by adding energy, such a drop may divide itself into two smaller drops...It seems therefore possible that the uranium nucleus has only small stability of form, and may, after neutron capture, divide itself into two nuclei of roughly equal size (the precise ratio of sizes depending on finer structural features and perhaps partly on chance).” A different form of fission, dubbed spontaneous fission because it occurs without bombardment by neutrons or any other projectiles, was reported by Flerov and Petrjak in a single-paragraph letter to *Physical Review* in 1940 [4]. For the remainder of this dissertation,

I will be referring mainly to spontaneous fission unless stated otherwise.

Fission is relatively simple to conceptualize, but remarkably difficult to explain quantitatively. Making fission predictions based on fundamental nuclear theory is challenging because of the large number of particles involved, along with the complex collective interactions which take place when one system deforms and becomes two. Historically, one could argue that theoretical attempts to describe nuclear fission have leapt forward in three major waves.

1.1.1 Liquid drop model

The first major wave of nuclear fission theory goes back to the very beginning of the nuclear age, with the liquid drop model in the 1930s. The liquid drop model was first developed by Weizsäcker in 1935 [5] as a way of describing the collective properties of nuclei. It was later adapted by Bohr and Wheeler to quantitatively describe nuclear fission in terms of bulk properties of nuclei [6]. This model was able to successfully describe nuclear binding energies and the energetics of nuclear fission.

The liquid drop model had its weaknesses, however. For example, it could not explain the fission fragment asymmetry which characterizes spontaneous fission in many actinides. Furthermore, until the 1960s, nuclear fission was treated as though separate from the rest of nuclear physics.

1.1.2 Strutinsky shell correction approach

The second theoretical wave came amidst a renewed interest in fission, triggered by the discovery of fission isomerism in 1962 by Polikanov, et al [7]. This was understood as a

manifestation of nuclear shape deformation based on a prediction by Nilsson [8]. In 1967, Strutinsky added a quantum mechanical correction to the liquid drop energy in order to account for the added stability that occurs when a nucleus contains a “magic number” of protons and/or neutrons [9–11]. These models go by the name “microscopic-macroscopic” because they combine the “macroscopic” bulk properties of the liquid-drop model with the “microscopic” quantum mechanical Strutinsky shell corrections.

These microscopic-macroscopic (“micmac”) fission models are computationally fairly inexpensive, and can achieve quite satisfactory results (some recent highlights from the Los Alamos and Warsaw groups include Refs. [12–15]). However, since the model is based on a phenomenological description of what is actually a quantum many-body system, its predictive power is limited, and there is no clear way of making systematic improvements. A more reliable approach would be to consider individual nucleon states using some kind of quantum many-body method.

1.1.3 Self-consistent models and the supercomputing era

The third major wave is taking place now, heralded by the age of supercomputers. Fission was listed in a recent 2017 report to the Department of Energy [16] as one of the problems which motivates the drive towards exascale computing. For large systems with many, many particles, density functional theory (DFT) is a way to recast the Schrödinger equation involving ~ 200 particles into a simpler problem involving only a few densities and currents (see Section 2.1.1). With DFT as a way of calculating nuclear properties quantum-mechanically, one can then combine self-consistent methods with modern high-performance computing platforms to predict fission properties, such as lifetimes and fragment yields. Fortunately, a great deal of work has been done to achieve exactly this (see a recent review article on

self-consistent approaches to fission in [17]). Some of the ideas which are used were inspired by lessons learned from micmac and other, simpler models; others are unique to DFT. One approach is described in detail in Chapter 2, and this is the model used to prepare this dissertation.

These advances in computing come simultaneously with advances in accelerator design and technology and other advances which allow experimental nuclear physics to reach far beyond what has been done before. For instance, the Facility for Rare Isotope Beams (FRIB) at Michigan State University is projected to be able to nearly double the number of isotopes that can be produced synthetically [18]. Together, state-of-the-art facilities for experiment and high-performance computing for theory are expected to lead to rapid advancement in our understanding of atomic nuclei and their decays.

1.2 Predicting fission fragments

Microscopic models (as self-consistent models are often called) are increasingly able to predict properties of fission fragments; however, a comprehensive description of fission fragments (including mass and fragment yields, excitation and kinetic energy distributions, angular dependence, spin, neutron emission) remains elusive in a microscopic framework. Chapter 2 will discuss one approach for describing the mass and charge of fission fragments. The challenge now is to do these calculations cheaply. In every theoretical calculation, one must ask oneself “What approximations can I safely make?” and “What are the important degrees of freedom for this problem?” One may also reduce the total time-to-answer via improvements to the computational workflow itself, such as better file handling and parallelization.

Additionally, static models are not well-suited to describing the process of a single nucleus

becoming two, in inherently time-dependent process. How can one precisely identify two distinct fragments when the wavefunctions of one fragment's constituent nucleons may extend into the opposite fragment? And how do those correlations between nucleons affect the energetics of the resulting fragments? A better understanding of the mechanism of fragment formation can help guide and refine fission fragment models.

1.3 Goals of the project

Historically, most experimental and theoretical studies of fission have centered around the region of actinides near ^{235}U , which includes isotopes of uranium, plutonium, and thorium relevant for reactor physics and stockpile stewardship. Isotopes in this region tend to fission asymmetrically, with the larger prefragment influenced by the shell structure of ^{132}Sn and resulting in a heavy fragment distribution centered around $\sim^{140}\text{Te}$. However, recent experiments have highlighted other forms of fission which take place in other regions of the nuclear chart.

Given the aforementioned recent interest in rare and exotic nuclei, we have applied our model to study spontaneous fission in exotic systems found in other regions of the nuclear chart, with a focus on primary fragment yields. First, in Chapter 4 we discuss bimodal fission in the neutron-deficient isotope ^{178}Pt , which until recently was conventionally expected to fission symmetrically. This region is a good one in which to test fission models because of the large isospin asymmetry ($N/Z \approx 1.3$ in this region, compared to $N/Z \approx 1.5$ near the valley of stability). Then in Chapter 5 we discuss cluster radioactivity in ^{294}Og , the heaviest element ever produced in a laboratory. In Chapter 6 we move to the neutron-rich side of the nuclear chart ($N/Z > 1.8$) to study isotopes which are expected to play a significant role in

the astrophysical r process.

This dissertation concludes in Chapter 7 with a discussion of results and their significance. Suggestions are then made for future model developments, computational improvements, and physical applications.

Chapter 2

Describing Fission Using Nuclear Density Functional Theory

Today there are two microscopic frameworks in which to study fission: time-dependent and static (time-independent). Time-dependent approaches evolve the system in real-time. Since fission is an inherently time-dependent process, these methods offer great insight into the fission process and the characteristics of the fragments, especially kinetic and excitation energies [19–23]. However, they can only treat a single event at a time and are quite expensive, making them impractical for fission yield predictions. Despite efforts such as [24, 25], there is currently no way to obtain a full yield distribution in a time-dependent framework.

More important to the present discussion, though, is the fact that time-dependent approaches are totally unsuited to spontaneous fission calculations. Spontaneous fission is fundamentally a quantum tunneling process, and at present there is no tunneling mechanism within time-dependent approaches. Furthermore, time-dependent computations tend to break down after too many time steps. Even if the tunneling problem was solved, this approach would still fail for any nucleus with a reasonably-long lifetime (compared to a typical time step size around $\sim 10^{-24}$ sec).

On the other hand, static approaches assume that collective motions of the nucleus are slow compared to the motion of the intrinsic particles, and therefore that collective and in-

trinsic degrees of freedom can be decoupled. This assumption, called the adiabatic approximation, is supported by experimental evidence which suggests a characteristic timescale for fission (from saddle to scission) of $\sim 10^{-20} - 10^{-18}$ sec, compared to typical nuclear timescales on the order of $\sim 10^{-22}$ sec (see [26] for a review of fission timescale experiments). The validity of the adiabatic assumption was further discussed for fission and other nuclear processes in [27].

The assumption of adiabaticity justifies the creation of a potential energy surface (PES) in some space of collective shape coordinates, and the dynamics of fission are then described as trajectories across the PES. Quantum tunneling pops out in a fairly natural way in this formalism, and half-life estimates follow. Calculating the kinetic and excitation energies in this framework is straightforward in principle, but in practice it is extremely sensitive to the scission configurations used [28]. However, the static approach is well-suited to estimating fission yields.

In an effort to be as self-consistent as possible, the PES is computed in the framework of nuclear DFT, which combines the Hartree-Fock-Bogoliubov (HFB) variational approximation to the energy with a many-body method inspired by Kohn-Sham DFT. An overview of this self-consistent mean-field framework is described below, followed by a description of the dynamical calculations which are used to calculate fission yields.

2.1 Nuclear density functional theory

Since nuclei are quantum systems, they can in principle be described using the Schrödinger equation. In practice, however, one finds this type of description difficult or impossible, for two reasons:

- In order to use the Schrödinger equation, one needs to describe the interaction between particles, in this case protons and neutrons. However, protons and neutrons are made up of quarks and gluons, which interact via the strong nuclear force. Consequently, an analytic expression for the nucleon-nucleon interaction (analogous to the $\frac{1}{r}$ form of the Coulomb interaction) is not available.
- Even if an interaction was known, nuclei are large systems made up of many protons and neutrons. Solving the Schrödinger equation directly quickly becomes computationally intractable as the number of nucleons increases.

Nuclear density functional theory is one of several methods which has been developed to address these challenges. It is particularly useful for heavy nuclei, where more precise *ab initio* methods become prohibitively expensive.

2.1.1 Density functional theory

Nuclear DFT is rooted in the Hohenberg-Kohn theorems [29], which follow.

Suppose a system is described in second quantization by a set of creation and annihilation operators c_i, c_i^\dagger which act on the vacuum state $|\psi_0\rangle$ to create single-particle states $c_i^\dagger |\psi_0\rangle$. Define the density: $\rho_{ij} = \langle \psi_0 | c_j^\dagger c_i | \psi_0 \rangle$. The first Hohenberg-Kohn theorem states that the energy of the system is a uniquely-defined functional of the density. That means that if a system of interacting particles and a system of noninteracting particles give the same density, the energy of those systems will be the same. This gives one the freedom to describe a system using a mean-field method instead of having to describe the pairwise interactions between each and every particle - a huge simplification!

The second Hohenberg-Kohn theorem states that the functional which gives the energy

of the system will give the ground state energy if, and only if, it acts on the true ground state density. Thus, given a particular functional, one can vary the input density to minimize the total energy and be assured that we are approaching the ground state energy of the system. A variational prescription was subsequently proposed by Kohn and Sham in [30], but because of the importance of pairing correlations in nuclear dynamics, we will instead use the HFB variational method. HFB mirrors the spirit of Kohn-Sham but with the inclusion of an additional pair density $\kappa_{ij} = \langle \psi_0 | c_j c_i | \psi_0 \rangle$, which can be thought of as a coupling between the vacuum state and a state with two particles (in states i and j). The pair density κ is combined with the single-particle density ρ to form a generalized density

$$\mathcal{R} = \begin{pmatrix} \rho & \kappa \\ -\kappa^* & 1 - \rho^* \end{pmatrix} \quad (2.1)$$

In coordinate space, the density matrix ρ and the pair tensor κ take the form

$$\rho(\vec{r}, \vec{r}') = \langle \psi_0 | c_{\vec{r}'}^\dagger c_{\vec{r}} | \psi_0 \rangle \quad (2.2)$$

$$\kappa(\vec{r}, \vec{r}') = \langle \psi_0 | c_{\vec{r}'} c_{\vec{r}} | \psi_0 \rangle \quad (2.3)$$

Note that in nuclei, there are two ρ s and two κ s: one set for describing neutrons and another for protons.

The next step is to find the correct energy density functional. Unfortunately, neither the Hohenberg-Kohn theorems nor the Kohn-Sham method specified how this is to be done. Typically at this point the total energy is divided into a sum of several contributions, which can each be treated individually:

$$E(\rho, \kappa) = E_{kin} + E_{Coul} + E_{nuc} + E_{pair} \quad (2.4)$$

where E_{kin} is the kinetic energy term, E_{Coul} contains the Coulomb interaction between protons, E_{nuc} is a nucleon-nucleon interaction term, and E_{pair} describes the tendency of nucleons to form pairs, which would otherwise be smeared out in non-interacting mean-field models. Portions of the energy density functional corresponding to each of these terms are described below.

2.1.1.1 Kinetic energy term

Defining the kinetic density $\tau_\alpha = \nabla \cdot \nabla' \rho_\alpha(\vec{r}, \vec{r}')|_{\vec{r}=\vec{r}'}$, $\alpha = p, n$, the kinetic energy contribution is

$$E_{kin} = \frac{\hbar^2}{2m} \left(1 - \frac{1}{A}\right) \int d^3\vec{r} (\tau_n(\vec{r}) + \tau_p(\vec{r})) \quad (2.5)$$

The $\left(1 - \frac{1}{A}\right)$ term is a simple, approximate center-of-mass correction.

2.1.1.2 Coulomb interaction term

The Coulomb interaction between protons is divided into a direct term and an exchange term, which is related to the antisymmetry of fermion wavefunctions:

$$E_{Coul} = E_{Coul,dir} + E_{Coul,exch} \quad (2.6)$$

$$E_{Coul,dir} = \frac{e^2}{2} \int d^3\vec{r}_1 d^3\vec{r}_2 \frac{\rho_p(\vec{r}_1)\rho_p(\vec{r}_2)}{|\vec{r}_1 - \vec{r}_2|} \quad (2.7)$$

$$E_{Coul,exch} = \frac{e^2}{2} \int d^3\vec{r}_1 d^3\vec{r}_2 \frac{\rho_p(\vec{r}_2, \vec{r}_1)\rho_p(\vec{r}_1, \vec{r}_2)}{|\vec{r}_1 - \vec{r}_2|} \quad (2.8)$$

Often the exchange term is computed in the Slater approximation [31, 32]:

$$E_{Coul,exch} \approx -\frac{3e^2}{4} \left(\frac{3}{\pi}\right)^{\frac{1}{3}} \int d^3\vec{r} \rho_p^{\frac{4}{3}}(\vec{r}) \quad (2.9)$$

2.1.1.3 Nuclear interaction term

Describing the interaction between nucleons E_{nuc} (and to a lesser extent, E_{pair}) continues to be an active area of research in nuclear theory today [33–37]. For nuclear DFT, the most commonly-used interactions belong to the Skyrme, Gogny, or covariant family of functionals (each of which is discussed in [38]). We will primarily be using Skyrme functionals, which can be written as a sum of both time-even and time-odd terms:

$$E_{Skyrme} = \int d^3\vec{r} \sum_{t=0,1} \left(\mathcal{H}_t^{even} + \mathcal{H}_t^{odd} \right) \quad (2.10)$$

$$\mathcal{H}_t^{even} = C_t^\rho \rho_t^2 + C_t^{\Delta\rho} \rho_t \Delta\rho_t + C_t^\tau \rho_t \tau_t + C_t^J \mathbf{J}_t^2 + C_t^{\nabla J} \rho_t \nabla \cdot \vec{J}_t \quad (2.11)$$

$$\mathcal{H}_t^{odd} = C_t^{s\bar{s}} \vec{s}_t^2 + C_t^{\Delta s} \vec{s}_t \Delta \vec{s}_t + C_t^T \vec{s}_t \cdot \vec{T}_t + C_t^j \mathbf{j}_t^2 + C_t^{\nabla j} \vec{s}_t \cdot (\nabla \times \vec{j}_t) \quad (2.12)$$

where τ_t is the kinetic energy density; \mathbf{J}_t is the spin current density, with vector part given by $\vec{J}_{\kappa,t} = \sum_{\mu\nu} \epsilon_{\mu\nu\kappa} \mathbf{J}_{\mu\nu,t}$; \vec{s}_t is the spin density, \vec{T}_t is the spin kinetic density; and \vec{j}_t is the

momentum density (to see how these are each related to ρ , see, e.g., [38]). The index $t = 0(1)$ refers to isoscalar(isovector) energy densities, e.g., $\rho_0 = \rho_n + \rho_p$ ($\rho_1 = \rho_n - \rho_p$). Note that \mathcal{H}_t^{even} depends only on time-even densities (and likewise for \mathcal{H}_t^{odd}).

Since this interaction is phenomenological, based on a zero-range contact interaction between nucleons, the coefficients are adjustable. There are dozens of Skyrme parameterizations on the market, each one optimized to a particular observable or set of observables. The parameter sets SkM* [39] and UNEDF1 [40] (along with its sister, UNEDF1_{HFB} [41]) are optimized to datasets which include fission data, making them suitable for fission calculations.

2.1.1.4 Pairing interaction term

The mean field approximation fails to take into account some correlations between nucleons, especially those which occupy similar states. Nucleons in nearby states (for example, with equivalent orbital quantum numbers but opposite spins) have a tendency to form pairs, similar to BCS superconductivity or ^3He superfluidity. To account for this phenomenon, we use a density-dependent pairing interaction:

$$E_{pair} = V_0 \int d^3\vec{r} \left(1 - \left(\frac{\rho(\vec{r})}{\rho_0} \right)^\alpha \right) \quad (2.13)$$

As with the nuclear interaction term, the pairing interaction contains several adjustable parameters V_0 , α , and ρ_0 . ρ_0 determines whether pairing takes place more within the volume ($\rho_0 \rightarrow \infty$), around the surface ($\rho_0 \approx 0.16 \text{ fm}^{-3}$), or somewhere in between. The exponent α affects the formation of surface effects, such as neutron skins and halos, but is usually set to $\alpha = 1$. The pairing strength V_0 may be adjusted to odd-even mass differences.

2.1.2 Hartree-Fock-Bogoliubov method

2.1.2.1 Bogoliubov transformation

In anticipation of the HFB formalism below, we define the so-called Bogoliubov transformation. The fundamental entity in the Bogoliubov transformed basis are ‘quasiparticle’ states, defined by quasiparticle creation and annihilation operators acting on a quasiparticle vacuum state $|\Phi_0\rangle$ (in contrast to the single particle operators from before). The creation and annihilation operators are given by

$$\beta_\mu = \sum_i U_{i\mu}^* c_i + \sum_i V_{i\mu}^* c_i^\dagger \quad (2.14)$$

$$\beta_\mu^\dagger = \sum_i U_{i\mu} c_i^\dagger + \sum_i V_{i\mu} c_i \quad (2.15)$$

or in block matrix notation,

$$\begin{pmatrix} \beta \\ \beta^\dagger \end{pmatrix} = \begin{pmatrix} U^\dagger & V^\dagger \\ V^T & U^T \end{pmatrix} \begin{pmatrix} c \\ c^\dagger \end{pmatrix} \equiv \mathcal{W}^\dagger \begin{pmatrix} c \\ c^\dagger \end{pmatrix} \quad (2.16)$$

where the transformation matrix \mathcal{W} must be unitary to ensure that β, β^\dagger obey the fermion commutation relations [42]. In this transformed basis, the density matrix takes the form

$$\mathbf{R} = \mathcal{W}^\dagger \mathcal{R} \mathcal{W} = \begin{pmatrix} \langle \Phi_0 | \beta_\mu^\dagger \beta_\nu | \Phi_0 \rangle & \langle \Phi_0 | \beta_\mu \beta_\nu | \Phi_0 \rangle \\ \langle \Phi_0 | \beta_\mu^\dagger \beta_\nu^\dagger | \Phi_0 \rangle & \langle \Phi_0 | \beta_\mu \beta_\nu^\dagger | \Phi_0 \rangle \end{pmatrix} = \begin{pmatrix} 0 & 0 \\ 0 & I_N \end{pmatrix} \quad (2.17)$$

2.1.2.2 HFB equations

The ground state configuration of the system described by this particular energy density functional E is described by the density which minimizes $E(\mathcal{R})$. We can find this solution through the variational principle. We minimize the energy with respect to the generalized density, subject to the constraint that $\mathcal{R}^2 = \mathcal{R}$, or in other words, that the state remains a quasiparticle vacuum. Defining the HFB Hamiltonian $\mathcal{H}_{ba} \equiv 2\partial E/\partial \mathcal{R}_{ab}$, this variation leads to the result $[\mathcal{H}, \mathcal{R}] = 0$, which is called the Hartree-Fock-Bogoliubov equation. It is not typically solved in this form, but it can be recast into something more useful. Recalling that two Hermitian operators whose commutator is zero can be simultaneously diagonalized, we choose to diagonalize \mathcal{H} using the same Bogoliubov transformation W which diagonalizes \mathcal{R} :

$$W^\dagger \mathcal{H} W \equiv \mathcal{E} \quad \text{or} \quad \mathcal{H} W = W \mathcal{E} \quad (2.18)$$

where

$$\mathcal{E} = \begin{pmatrix} E_\mu & 0 \\ 0 & -E_\mu \end{pmatrix} \quad (2.19)$$

is a matrix of quasiparticle energies. In this form, the problem can then be solved iteratively: an initial density ansatz is chosen in order to construct the Hamiltonian density \mathcal{H} , after which the eigenvalue problem is solved, leading to new densities (since the densities are related to \mathcal{W}), which in turn leads to an updated \mathcal{H} . This procedure can be repeated indefinitely, until some predetermined convergence criterion is met.

Very often we will want to minimize the energy with the system subject to a particular

constraint. In that case we would replace the Hamiltonian E with the Routhian E' before variation. Typically E' introduces the constraints via the method of Lagrange multipliers. Some common examples might be this simple form of particle number restoration (more sophisticated forms, such as Lipkin-Nogami \cite{???}, also exist)

$$E' = E - \lambda_n \langle \hat{N}_n \rangle - \lambda_p \langle \hat{N}_p \rangle \quad (2.20)$$

where λ_α is determined later by the condition that $\langle \hat{N}_\alpha \rangle = N_\alpha$, or shape, where we might constrain a particular multipole moment (or set of multipole moments) to the value $\bar{Q}_{\lambda\mu}$

$$E' = E - \sum_{\lambda\mu} C_{\lambda\mu} \left(\langle \hat{Q}_{\lambda\mu} \rangle - \bar{Q}_{\lambda\mu} \right)^2 \quad (2.21)$$

2.1.3 Nucleon localization function

One of the tools we will be using quite a bit in this thesis is the nucleon localization function (NLF), introduced in [43]. The NLF is defined using the single particle density in the following way (with q =isospin and σ =spin/signature quantum number):

$$\mathcal{C}_{q\sigma} = \left[1 + \left(\frac{\tau_{q\sigma} \rho_{q\sigma} - \frac{1}{4} |\nabla \rho_{q\sigma}|^2 - \mathbf{j}_{q\sigma}^2}{\rho_{q\sigma} \tau_{q\sigma}^{TF}} \right)^2 \right] \quad (2.22)$$

where $\tau_{q\sigma}^{TF} = \frac{3}{5} (6\pi^2)^{\frac{2}{3}} \rho_{q\sigma}^{\frac{5}{3}}$. A localization value $\mathcal{C} \approx 1$ means that nucleons are well-localized; that is, the probability of finding two nucleons of equal spin and isospin at the same location in space is low. A value of $\mathcal{C} = \frac{1}{2}$ corresponds to a Fermi gas of nucleons, as found in nuclear matter.

The NLF offers greater insight into the underlying shell structure of the system than,

for instance, the single particle density. In particular, when applied to fission as in [44], it sometimes enables one to see the formation of well-defined prefragments whose shell structure is responsible for the peak of the fragment distribution. A method for identifying fission fragments and estimating fragment distributions using the NLF is described in Appendix A.

2.2 Microscopic description of nuclear fission

With the nuclear physics somewhat under control, we now move onto the problem of using it to describe fission. Recently in [45], an approach based on this assumption was used to compute fragment yields from a potential energy surface (PES) that was computed self-consistently, using the WKB approximation to describe the tunneling and Langevin dynamics to describe post-scission dissipation. The half-life can be computed as in [46].

2.2.1 Potential energy surfaces

In the adiabatic approximation, the primary degrees of freedom are nuclear shapes, and therefore the basic ingredient to fission calculations is a potential energy surface (PES). In principle, one could describe any three-dimensional shape using an infinite basis such as the multipole expansion which is often encountered in electrodynamics; however, for practical computations one must use a truncated set of only a few collective coordinates. Thus, an important challenge for researchers is to select the most relevant collective coordinates, ideally while demonstrating that others can be safely neglected. Often one will use the first few lowest-order multipole moments; however, multipole moments may not always be well-suited to describing shapes which occur during fission, especially near scission. One alternative was proposed in [?].

Once the appropriate shape constraints are chosen, the PES is computed as a mesh: one DFT calculation per grid point. The value at each point is the HFB energy computed above, $E'(\vec{q})$.

2.2.2 Collective inertia

Just as important to the fission dynamics as the energy of the system is the collective inertia, which describes the tendency of the system to resist configuration changes (such as shape changes). The form of the collective inertia we use is the non-perturbative adiabatic time-dependent HFB (ATDHFB) inertia with cranking [47], which takes the form

$$M_{\mu\nu} = \frac{\hbar^2}{2} \frac{1}{(E_a + E_b)} \left(\frac{\partial \mathcal{R}_{(0),ab}^{21}}{\partial q_\mu} \frac{\partial \mathcal{R}_{(0),ba}^{12}}{\partial q_\nu} + \frac{\partial \mathcal{R}_{(0),ab}^{12}}{\partial q_\mu} \frac{\partial \mathcal{R}_{(0),ba}^{21}}{\partial q_\nu} \right) \quad (2.23)$$

The subscripts and superscripts are explained in the full temperature-dependent derivation of the collective inertia found in Appendix B, but the important feature to note is that computing the inertia requires differentiating the density matrix with respect to a set of collective coordinates.

A perturbative expression for the ATDHFB inertia also exists, which allows one to estimate the inertia without taking derivatives of the density. It is computationally much faster and easier to implement, but it is less accurate and loses many of the important features of the inertia, as we shall see in Chapter 5. Nevertheless, it is commonly-used in calculations and we shall use it later on.

Another common expression for the collective inertia comes from the Generator Coordinate Method (GCM). The GCM inertia also exists in two varieties: perturbative and non-perturbative [48]. Like the ATDHFB inertia, the perturbative GCM inertia is smoothed-

out compared to the non-perturbative inertia. Both the perturbative and non-perturbative GCM inertias are found to be smaller in magnitude than their ATDHFB counterparts.

2.2.3 WKB approximation

Spontaneous nuclear fission is a type of quantum tunneling; consequently, it should be described using quantum mechanics. If the wavefunction corresponding to the fissioning nucleus is assumed to be slowly-varying inside the potential barrier (which is the case under the adiabatic assumption), then the WKB approximation allows us to estimate the tunneling probability through a classically-forbidden region in the PES.

Consider a set of collective coordinates $\mathbf{q} \equiv (q_1, \dots, q_N)$. The most-probable tunneling path $L(s)|_{s_{\text{in}}}^{s_{\text{out}}}$ in the collective space is found via minimization of the collective action

$$S(L) = \frac{1}{\hbar} \int_{s_{\text{in}}}^{s_{\text{out}}} \sqrt{2\mathcal{M}(s)(V(s) - E_0)} ds, \quad (2.24)$$

where s is the curvilinear coordinate along the path L , $\mathcal{M}(s)$ is the collective inertia given by [46]

$$\mathcal{M}(s) = \sum_{\mu\nu} M_{\mu\nu} \frac{dq_\mu}{ds} \frac{dq_\nu}{ds} \quad (2.25)$$

and $V(s)$ is the potential energy along $L(s)$. E_0 stands for the collective ground-state energy. The dynamic programming method [49] is employed to determine the path $L(s)$. The calculation is repeated for different outer turning points, and each of these points is then assigned an exit probability $P(s_{\text{out}}) = [1 + \exp\{(2s)\}]^{-1}$ [50].

The half-life corresponds to the minimum action pathway, and the expression for the half-life is $T_{1/2} = \ln(2)/nP(s_{\text{min}})$. The parameter n is the number of assaults on the fission

barrier per unit time and the standard value is $n = 10^{20.38} s^{-1}$.

2.2.4 Langevin dynamics

the region of Langevin dynamics, which is the region connecting the hypersurface of outer turning points and to the hypersurface of scission points,

Two techniques for predicting fission fragment yields are the Langevin approach used by [45] and the Time-Dependent Generator Coordinate Method (TDGCM) approach used in [?]. I will be using Langevin dynamics, which are described in this section.

After emerging from the classically-forbidden region of the PES, fission trajectories begin from the outer turning line and then evolve along the PES according to the Langevin equations:

$$\frac{dp_i}{dt} = -\frac{p_j p_k}{2} \frac{\partial}{\partial q_i} \left(\mathcal{M}^{-1} \right)_{jk} - \frac{\partial V}{\partial q_i} - \eta_{ij} \left(\mathcal{M}^{-1} \right)_{jk} p_k + g_{ij} \Gamma_j(t), \quad (2.26)$$

$$\frac{dq_i}{dt} = \left(\mathcal{M}^{-1} \right)_{ij} p_j, \quad (2.27)$$

where p_i is the collective momentum conjugate to q_i . The dissipation tensor η_{ij} is related to the random force strength g_{ij} via the fluctuation-dissipation theorem, and $\Gamma_j(t)$ is a Gaussian-distributed, time-dependent stochastic variable.

The fluctuation-dissipation theorem is given by the expression $\sum_k g_{ik} g_{jk} = \eta_{ij} k_B T$. It effectively couples the collective and intrinsic via the system temperature, given by $k_B T = \sqrt{E^*/a}$ where $a = A/10 \text{ MeV}^{-1}$ parameterizes the level density and the excitation energy $E^* = V(s_{out}) - V(\mathbf{x}) - \frac{1}{2} \sum (\mathcal{M}^{-1})_{ij} p_i p_j$.

Dissipation is treated in our work as a parameter, as a self-consistent description of dissipation is not yet known. However, work along this line has been started (maybe?) in

refs 291-293 of [51] (see Section 4.1.1 for the context). In the meantime, we use the values from [45] (Is this too specific for a thesis? You're not worried about the little numerical details, right? Just the big-picture ideas?)

Chapter 3

Numerical Implementation

Since this modern era of fission theory takes advantage of high-performance computers, it is worth taking some time to discuss some of the issues which came up during the course of this research, and how modern computing tools were used to solve the problem.

3.1 Calculating the PES

By far, the most time-intensive part of a microscopic fission calculation is the calculation of the PES. For this we use a pair of DFT solvers, HFODD [52] and HFBTHO [53]. These programs solve the HFB equations in a basis of deformed harmonic oscillators. The solver HFBTHO is limited to shapes with axial symmetry, while HFODD allows for the breaking of any symmetry needed. Broken symmetries mean that each matrix element must be computed independently, while good symmetries mean However, since the major bottleneck of each of these programs involves constructing matrices representing Skyrme densities and currents and then diagonalizing the matrix representing the HFB Hamiltonian, this flexibility drastically increases the time-to-solution.

On the positive side, the problem of calculating a PES is embarrassingly-parallel. So while an individual point in the PES may be difficult to compute, many points can be computed simultaneously. This does have its limitations; highly-deformed configurations may be very unstable because of reasons. One fix may sometimes be to use a nearby point

which converged successfully as a seed function

The procedure is performed iteratively: First, an ansatz is given for the density (either by the user or by some simple means, such as a quick Woods-Saxon calculation). Then the energy density matrix is constructed, after which it is diagonalized and a new density matrix is calculated. The procedure then repeats for a fixed number of iterations, or until a predetermined convergence criterion is satisfied. In HFODD, for instance, the default convergence criterion is for the difference between the HFB energy and the total energy summed over all single-particle states to be less than some user-defined value.

3.1.1 PES Tools

Apart from the issue of walltime, generating a PES creates a lot of output files, which quickly becomes unwieldy. To help manage all this data, a Python module called PES Tools was created for manipulating, extracting, interpolating, and plotting PES data [54]. Aside from solver-dependent parser scripts, which collect data from the output of a DFT run and store it in the XML file format, PES Tools is not dependent on a particular DFT solver.

In particular, a submodule was created to interface between PES Tools and Fission Tools [55], a set of codes which have relevance to fission calculations. Many of these codes are described in the following sections.

3.2 Calculating the collective inertia

The partial derivatives from equation 2.23 are computed using the Lagrange three-point formula:

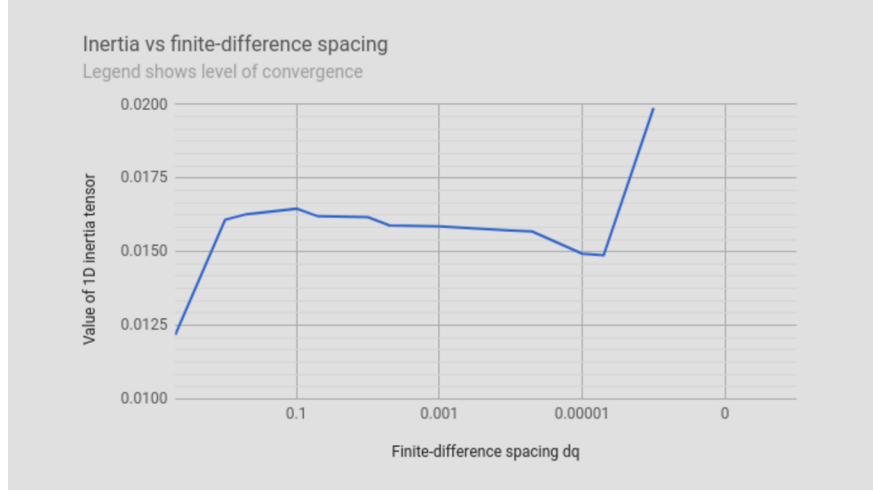


Figure 3.1: \mathcal{M}_{22} calculated for an arbitrary configuration of ^{240}Pu as a function of finite-difference spacing.

$$\left(\frac{\partial \mathcal{R}}{\partial q}\right)_{q=q_0} \approx \frac{-\delta q'}{\delta q (\delta q + \delta q')} \mathcal{R}(q_0 - \delta q) + \frac{\delta q - \delta q'}{\delta q \delta q'} \mathcal{R}(q_0) + \frac{\delta q}{\delta q' (\delta q + \delta q')} \mathcal{R}(q_0 + \delta q') \quad (3.1)$$

The accuracy and precision of the collective inertia \mathcal{M} are therefore functions of the spacings δq and $\delta q'$, and of \mathcal{R} . An accurate value of the collective inertia is especially important for computing half-lives, where there is an exponential dependence on \mathcal{M} .

Figure 3.1 shows the effect of different values of $\delta q = \delta q'$ on the collective inertia for an arbitrary configuration of ^{240}Pu .

Figure 3.1 shows the norm of the matrix which corresponds to the difference between the density matrix at the last iteration and the second-to-last iteration. Predictably, the norm decreases as the convergence parameter becomes tighter. This gives a sense of the uncertainty associated with the density, which in turn should be propagated through equations 3.1 and 2.23.

There are additional complications which arise in the finite-temperature formalism. These

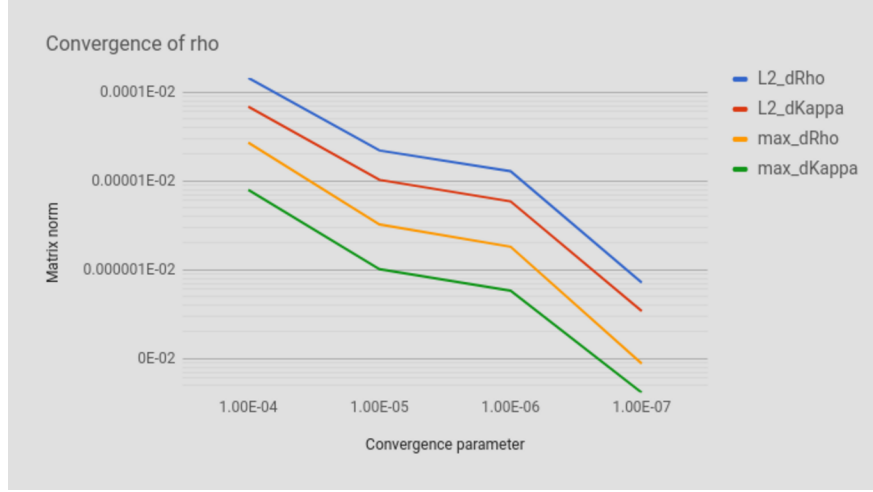


Figure 3.2: Norm of the difference matrix between subsequent iterations of the density.

are discussed in Appendix B.

3.3 Minimum action path

For the tunneling described in Section 2.2.3, the dynamic programming method [49] was used to minimize the action. The dynamic programming scheme proceeds inductively: Once the minimum action is known for all grid points up to a certain value of Q_{20} , say q_{20}^n , then the minimum action at each grid point in the layer with $Q_{20} = q_{20}^{n+1}$ is obtained by computing the action between each grid point in layer n and each grid point in layer $n + 1$, and then finding the path which minimizes the total action at each grid point in layer $n + 1$:

$$S_{min}(\vec{Q}) \Big|_{Q_{20}=q_{20}^{n+1}} = \operatorname{argmin}_{\vec{Q}'} \left(S_{min}(\vec{Q}') + \Delta S_{min}(\vec{Q}, \vec{Q}') \right) \Big|_{Q'_{20}=q_{20}^n, Q_{20}=q_{20}^{n+1}}. \quad (3.2)$$

The inductive step which connects layers n and $n + 1$ involves several small, independent calculations which lend themselves well to shared-memory parallelism. This was implemented

in the code using OpenMP, resulting in a walltime reduction from order $\mathcal{O}(n^D)$ to $\mathcal{O}(n^D/m)$, where m is the number of processors (with the usual caveats that parallelization requires some additional overhead time, and that the actual speedup might be somewhat less when the number of processors m reaches the same order as the number of points per layer n^{D-1}). In a 2D calculation, where the runtime is on the order of seconds, the difference is inconsequential. However, this speedup was essential for the analysis of a 4D PES, as described in Chapter 5.

3.4 Langevin

Once the action and relative probability are known for a set of points along the outer turning line, Langevin trajectories are computed originating from each outer turning point. These are straightforwardly evaluated at discrete time steps over a discretized PES mesh.

Because of the random force term in equation 2.26, a large number of trajectories per outer turning point must be computed to reduce statistical uncertainty. Fortunately, each trajectory is completely independent of every other trajectory, lending the code readily to shared-memory parallelism. However, for the Fission Tools Langevin code, distributed-memory parallelism was chosen over shared-memory parallelism in order to simplify access to shared resources, such as variables and output files.

Chapter 4

Two fission modes in ^{178}Pt

4.1 Asymmetric fission in the region of ^{180}Hg

As mentioned in the introduction, fission has been studied most carefully in the region of the actinides ($Z=90$ to $Z=103$), as many naturally-occurring isotopes in this region are fissile. Within this region, there is a characteristic tendency for fission fragment yields to be asymmetric (that is, one light fragment and one heavy fragment), with the heavy peak centered around $A \approx 140$. This has been understood as a manifestation of nuclear shell structure in the prefragments: doubly-magic ^{132}Sn drives the nucleus towards scission, and once the neck nucleons are divided up between the two fragments, the heavy fragment distribution peaks near $A=140$. As one moves to the lower- Z actinides, however, this tendency becomes less and less pronounced as yields tend to become more symmetric. Until recently, it was generally believed that below thorium, yields would continue to be symmetric. For sub-thorium isotopes, there was no doubly-magic nucleus candidate that could drive the system toward asymmetry as there is with actinides. To the contrary: neutron-deficient ^{180}Hg , for instance, might be expected to split evenly into two ^{90}Zr fragments, each with $N=50$ closed shells.

However, it was reported in a 2010 study [56] that neutron-deficient ^{180}Tl undergoes beta-delayed fission, leading to intermediate state ^{180}Hg which then decays into two fragments of unequal mass. This finding triggered a flurry of theoretical papers hoping to describe

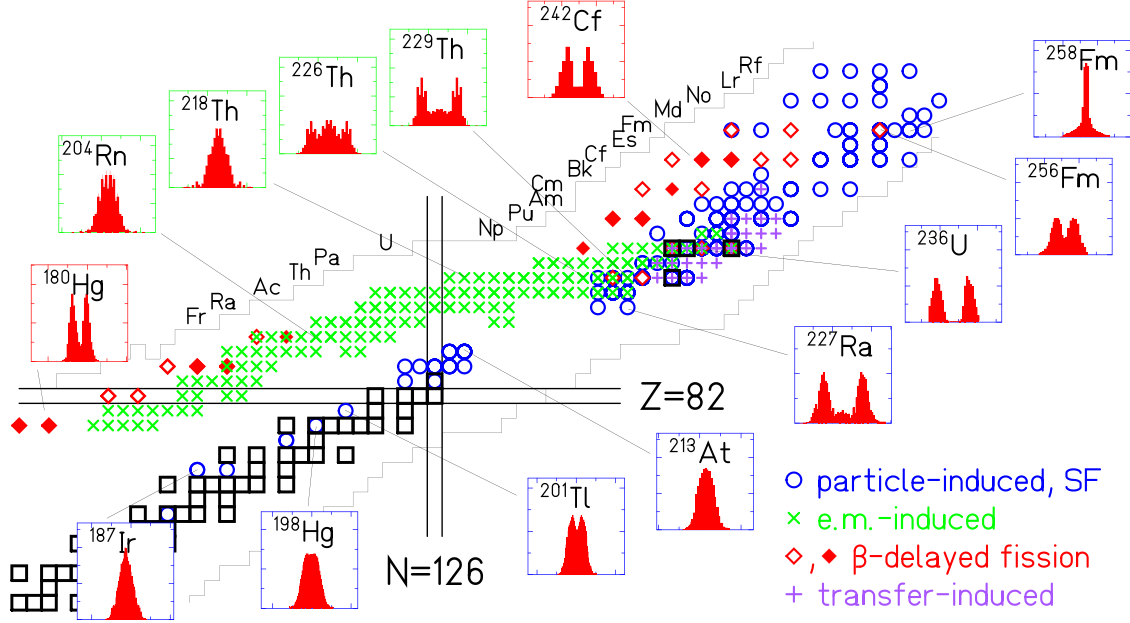


Figure 4.1: Fragment yields for several nuclei ranging from actinides, where primary fission yields tend to be asymmetric, down to near-thorium, where yields become more symmetric, and finally to the region near neutron deficient ^{180}Hg , where asymmetry returns. Figure from [62].

this new and unexpected phenomenon (for instance, see [57–60]). A follow-up study using ^{178}Tl [61] further established this as a region of asymmetric fission, and not just a one-time occurrence. Since then, other nuclei in the region have been studied using a variety of reactions and techniques, and the finding is the same.

Later experiments have shown that, unlike the case of actinides where shell structure and fragment asymmetry are “washed out” at high excitation energies, mass asymmetric fragment distributions are a persistent feature of this mass region for various excitation energies (see [62] and references therein). An overview of nuclei in the region of ^{180}Hg which have been experimentally studied (as of 2016), including the experimental technique used, is shown in Figure 4.1.

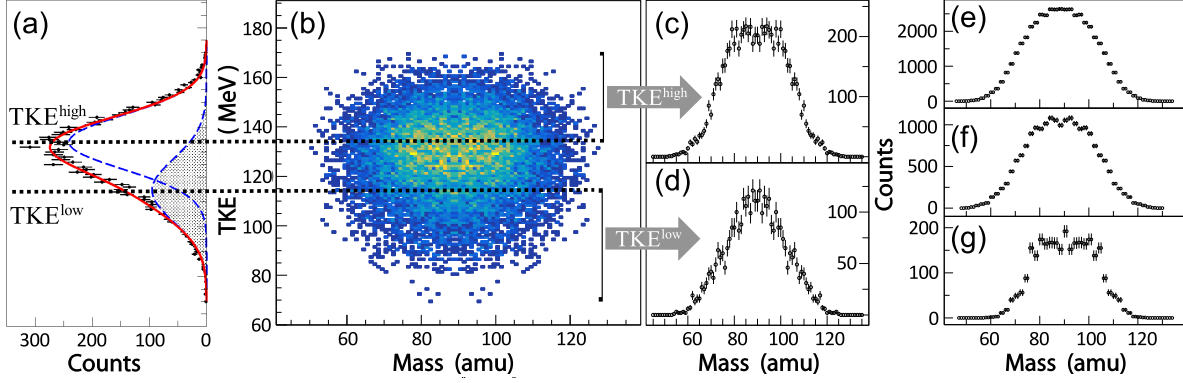


Figure 4.2: After projecting the fission fragment mass vs total kinetic energy (TKE) correlation (a) onto the TKE axis, the TKE distribution is deconvoluted into high- and low-energy components, centered around the values TKE^{high} and TKE^{low} (b). The corresponding mass distributions are fitted to a double (c) and single (d) Gaussian, respectively. This procedure is repeated for three different compound nucleus excitation energies E^* (e-g). Figure from [63]

4.2 Multimode fission of ^{178}Pt

One particular follow-up experiment was performed to investigate the spontaneous fission of ^{178}Pt [63], which differs from ^{180}Hg by 2 protons. This system was studied at various excitation energies and found to fission consistently in a bimodal pattern, as shown in Figure 4.2. Of the sample measured, roughly 1/3 of cases were found to fission symmetrically, while the other 2/3 fissioned asymmetrically with a light-to-heavy mass ratio of approximately 79/99. Furthermore, it was observed that mass-asymmetric fragments tended to have higher kinetic energies than symmetric fragments.

To better interpret the results of this experiment, DFT calculations were performed using the functionals UNEDF1_{HFB} [41] and D1S [64]. These calculations involved computing a PES using the collective coordinates Q_{20} and Q_{30} . The UNEDF1_{HFB} PES is shown in Figure 4.3, while the D1S PES is in Figure 4.4. A calculation with full Langevin dynamics was not performed; however, the static (minimum-energy) pathways shown in the figures correspond to a fragment split $A_L/A_H \approx 80/98$.

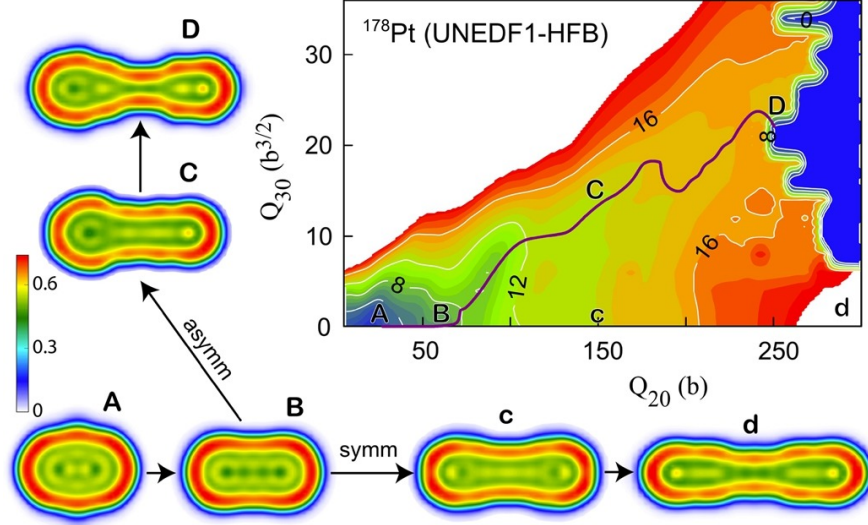


Figure 4.3: UNEDF1-HFB potential energy surface for ^{178}Pt . Note the two different trajectories ABCD and ABcd and their corresponding NLFs.

Also shown in Figure 4.3 are nucleon localization functions (recall Section 2.1.3) corresponding to various marked configurations in the PES. Along the symmetric path (ABcd in the figure), the fragments appear highly-elongated, even shortly before scission. Since elongation tends to minimize the Coulomb repulsion between fragments, then this configuration might be expected to lead to fragments with relatively low kinetic energies. On the other hand, compact fragments such as those in ABCD will tend to have a larger Coulomb repulsion. Fragments will be propelled away from one another with greater force, resulting in fragments with a higher kinetic energy, which is in qualitative agreement with experiment.

Comparing the UNEDF1_{HFB} PES in Figure 4.3 to the D1S PES in Figure 4.4a, one may note that, despite the inherent differences between the functionals, the overall topology of the PES is similar in both cases. In fact, the topology in both cases is quite flat, which suggests (in agreement with the observed data) the possibility of a competition between symmetric and asymmetric fission modes. Additionally, as shown in Figure 4.4b, there appears an additional channel corresponding to compact symmetric fragments. This channel is higher

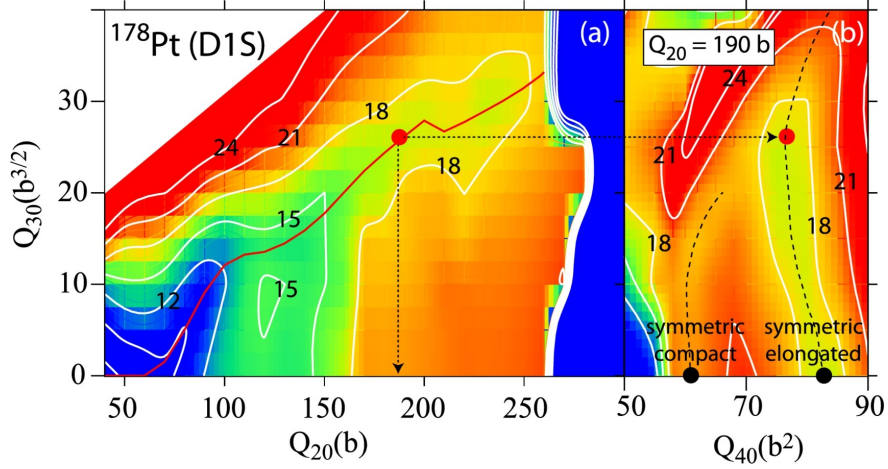


Figure 4.4: D1S potential energy surface for ^{178}Pt . Note also the additional information about the hexadecapole moment.

in energy than the elongated symmetric pathway and is blocked by a ~ 4 MeV saddle point, but it is conceivable that this channel might be more easily accessed by other isotopes in this region.

4.3 The physical origin of fragment asymmetry in the neutron-deficient sub-lead region

By now it is now well-established that many isotopes in the neutron-deficient sub-lead region will fission asymmetrically. Microscopic-macroscopic calculations correctly predict asymmetry in the yields, and static DFT calculations do even better, able to predict the peak of the distribution to within 1-2 nucleons. In that sense, it may be said that the phenomenon is understood. That said, a simple interpretation or explanation of that phenomenon is still a matter of some debate.

In one of the earliest theoretical responses to the discovery of asymmetric fission in ^{180}Hg [58], it is argued that the best explanation for the observation, however unsatisfying, is simply

the sum total of all the physics that gets wrapped together to compute a PES. Fragment yields are given by subtle interplays in local regions of the potential energy surface, while magic number-based arguments are basically just hand-waving that has fortuitously worked out in the region of actinides. The fact of asymmetric fragments, in this explanation, is something that happens in spite of, and not because of, fragment shell effects (which, two of the authors later note [65], are rather weak in this region).

By contrast, it is argued in [66] that the fragment masses are determined by the shell structure of two well-formed prefragments connected by a thin neck. The nucleons from the neck are then redistributed to either of the prefragments somewhere along the way from saddle point to scission. This argument was further reinforced in a follow-up paper [59], in which it is shown that the asymmetric path is associated with stronger shell effects than the symmetric path.

A more recent paper [67] fundamentally agrees with this perspective, except they argue that one should consider the shell structure of octupole-deformed prefragments instead of those with spherical symmetry. By their reasoning, octupole correlations would favor fragment distributions with $Z_{light} \approx 34$ and $N_{heavy} \approx 56$.

Most recently, an argument is presented in [60] which likewise invokes deformed shell gaps; however, in this case the argument is made for octupole-deformed (or rather, mass asymmetric) parent nuclei, as opposed to octupole-deformed fragments.

Taken together, these suggest that fragment asymmetry is the result of a coupling between highly-deformed shell gaps in the parent nucleus and (possibly-deformed) shell gaps in the fragment nuclei. The separation process might also introduce some additional messiness, which may involve dissipation and particle emission.

It is worth noting that, so far, no microscopic dynamical description has been given for

fission in this region. It would be interesting to see how the collective inertia behaves for these nuclides, and how it affects the dynamics.

Chapter 5

Cluster decay in ^{294}Og

5.1 Cluster emission in superheavy elements

The region of superheavy elements (SHEs), defined as the set of nuclides with $Z > 104$, is an interesting one for the study of spontaneous fission because the liquid drop model predicts that all isotopes with $Z > 104$ are unstable with respect to spontaneous fission. These nuclei are stabilized due to shell effects, but they nevertheless remain short-lived and many of them will decay by spontaneous fission regardless.

Experimentally, spontaneous fission has been observed from several superheavy isotopes (see the right panel of Figure 5.1). Other observed SHEs undergo a decay chain with several alpha decays, followed by spontaneous fission. Furthermore, a variety of models predict regions of spontaneous fission in the superheavy regime. One example is shown in Figure 5.1, in which branching ratios were estimated by computing and comparing different decay lifetimes from empirical formulas. Figure 5.2 is similar, except that the spontaneous fission lifetimes were computed microscopically, as were the Q_α values used to estimate alpha decay lifetimes.

This still leaves open the question of fission fragments, however. Several authors have predicted, using models both phenomenological [69–75] and microscopic [76], that some SHEs will undergo a highly-asymmetric form of fission in which the parent nucleus decays into two

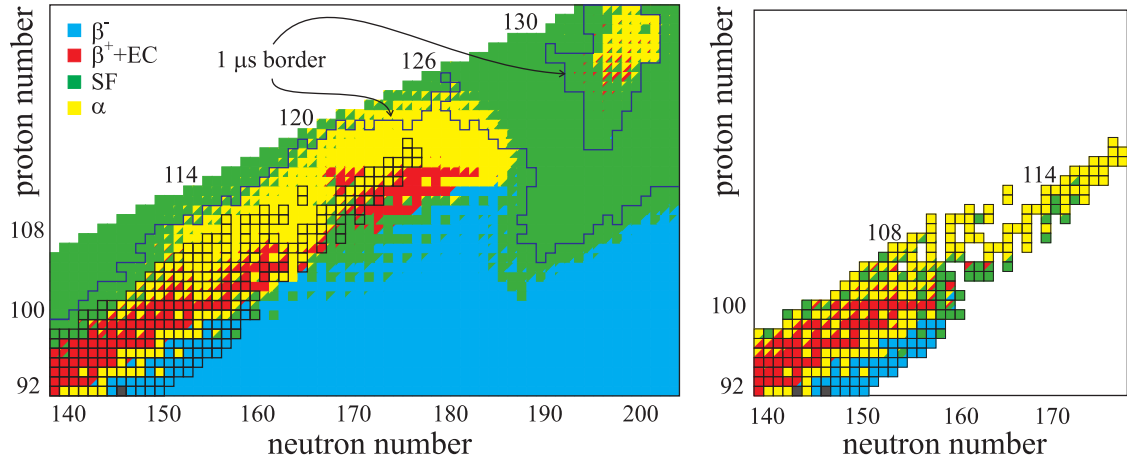


Figure 5.1: Calculated (left) and experimental (right) decay modes for SHE, based on an analysis of lifetimes calculated via empirical formulae. The boxed isotopes in the left panel are those which have been measured experimentally. Isotopes falling inside the $1\mu\text{s}$ contour are predicted to live longer than $1\mu\text{s}$. Figure adapted from [68].

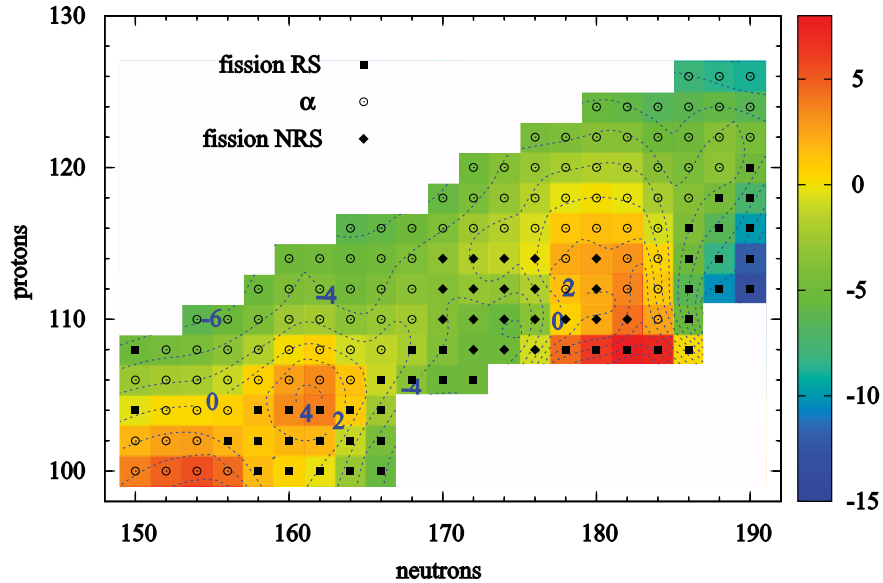


Figure 5.2: Dominant decay modes for SHE in a nuclear DFT-based framework are indicated. The label “RS” stands for “reflection symmetric” and “NRS” stands for “non-reflection symmetric.” The colorbar indicates the predicted half-life on a logarithmic scale. Figure from [57].

fragments, with the heavy fragment near the doubly-magic nucleus ^{208}Pb . This particular decay mode is significant enough to have earned its own name in the literature, where it is known variously as cluster emission, cluster radioactivity, or lead radioactivity [77–81]. The phenomenon of cluster emission was first observed in 1984 in the decay $^{223}\text{Ra} \rightarrow ^{209}\text{Pb} + ^{14}\text{C}$ [82] and has since been observed in several actinides. In all cases seen so far, it is a rare event with a small branching ratio [80].

The mechanism of cluster emission is based on the stability of the doubly-magic nucleus ^{208}Pb . ^{294}Og is a particularly excellent candidate for cluster emission because the cluster it is predicted to emit, ^{86}Kr , receives additional stability due to its having a magic number of neutrons. Semiempirical arguments based on the symmetry energy lend additional support to this candidate, since ^{294}Og and ^{208}Pb have a similar N/Z ratio [76].

We took this prediction one step further by calculating the full spontaneous fission fragment distribution of ^{294}Og . As will be shown, the distribution is sharply-peaked around ^{208}Pb , and this will be shown to be quite robust with respect to various inputs. A visualization of the process using the NLF shows strong evidence of a ^{208}Pb prefragment being formed early in the post-saddle stage of the evolution.

5.2 Predicted spontaneous fission yields of ^{294}Og

Potential energy surfaces were computed for each of three EDFs: UNEDF1_{HFB} [41], a Skyrme functional which was optimized to data for spherical and deformed nuclei, including fission isomers; SkM* [39], another Skyrme functional designed for fission barriers and surface energy; and D1S [64], a parameterization of the finite-range Gogny interaction fitted on fission barriers of actinides. A comparison of the different two-dimensional PESs is shown

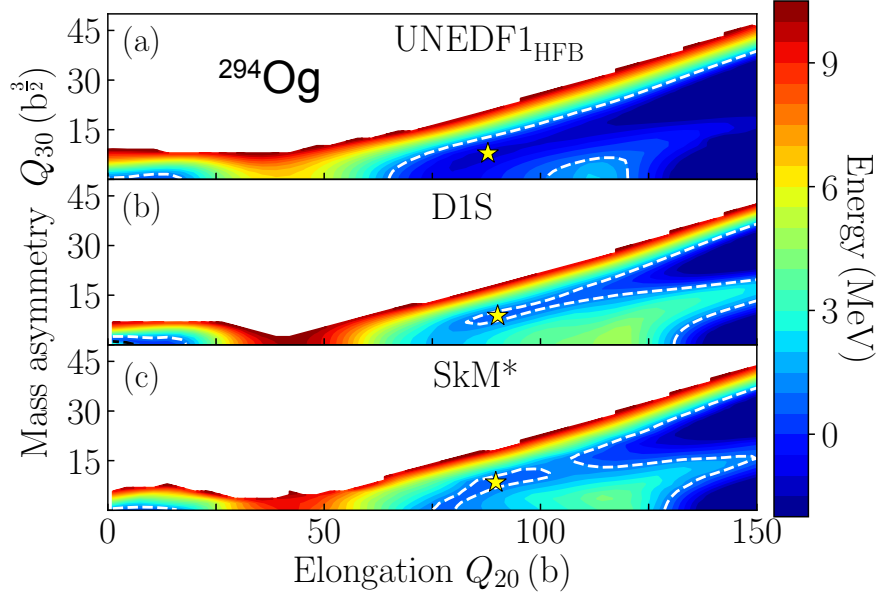


Figure 5.3: Comparison of the PESs for ^{294}Og in the (Q_{20}, Q_{30}) collective plane obtained in UNEDF1_{HFB} (a), D1S (b), and SkM* (c) EDFs. The ground-state energy E_{gs} is normalized to zero. The dotted line in each figure corresponds to $E_0 - E_{gs} = 1$ MeV, which was used to determine the inner and outer turning points. The local energy minima at large deformations are marked by stars.

in Figure 5.3. Despite the differences between the functionals, it is reassuring to see that the surfaces strongly resemble one another. Some common features we highlight are: a symmetric saddle point occurring around $Q_{20} \approx 40$ b; a second barrier beginning around $Q_{20} \approx 100 - 120$ b along the symmetric fission path; the presence of local minima at large deformations (marked by stars in the figure); a deep valley that leads to an highly-asymmetric split; and the secondary, less-asymmetric fission valley that emerges at large elongations.

But there are differences as well, such as the height of the first saddle point, the depth of the highly-asymmetric fission valley, and the height of the ridge separating the two fission valleys. As a result, the outer turning points are pushed to larger elongations in D1S and SkM* as compared to UNEDF1_{HFB}. These differences in the PES topology strongly affect the predicted spontaneous fission half-lives τ_{SF} , which in the case of UNEDF1_{HFB}, SkM* and D1S are 9.1×10^{-9} s, 4.0×10^{-5} s and 3.2×10^{-2} s, respectively (see also [83, 84] for

a detailed discussion of half-lives). These large variations of τ_{SF} reflect the well-known exponential sensitivity of spontaneous fission half-lives to changes in the quantities entering the collective action (2.24). The τ_{SF} predictions of UNEDF1_{HFB} and, to a lesser degree, SkM* are incompatible with experiment, as ^{294}Og is known to decay by α -decay with a half-life of 0.58 ms [85]. This observation could in fact also apply to the D1S results, since the D1S calculations were performed in a smaller collective space leading to overestimation of the half-lives [86, 87].

It is to be noted that while half-lives are very sensitive to details of the calculations, the models used here are very consistent with each other and with experiment when it comes to global observables, such as alpha-decay energies, deformations, and radii [88, 89]. It will be demonstrated below that spontaneous-fission mass and charge yields are also robustly predicted. This will be shown by varying the EDF, the collective space, the collective inertia, and the strength of the Langevin dissipation tensor.

The EDF and the collective space were varied together; a different collective space was used for each EDF in the tunneling portion of the PES. The UNEDF1_{HFB} calculation was carried out in a four-dimensional collective space consisting of the collective coordinates $(Q_{20}, Q_{30}, Q_{22}, \lambda_2)$. By examining this PES, we were able to reduce to dimensionality of the PES for the other two functionals. The SkM* calculation was performed in a piecewise-continuous space. Between the ground state and the isomer state, Q_{30} does not play a significant role and so the system was described using $(Q_{20}, Q_{22}, \lambda_2)$. Likewise, $Q_{22} \approx 0$ once the isomer state is reached and reflection symmetry is broken ($Q_{30} \neq 0$), suggesting use of the coordinates $(Q_{20}, Q_{30}, \lambda_2)$. Finally, for the functional D1S we decided to see how our yields would be affected if we did not consider dynamical pairing fluctuations or axial symmetry breaking at all, which results in a drastic reduction to computation time. Those

calculations were performed in the collective space (Q_{20}, Q_{30}) .

In the region of Langevin dynamics, we found again that $Q_{22} \approx 0$. Consequently, this region was limited to two dimensions (Q_{20}, Q_{30}) in all cases.

The resulting yields are shown in Figure 5.4. As expected, the yields are peaked in the region of ^{208}Pb with a sharp fall-off. Likewise, the projected distributions onto the mass and charge axes shows a clear preference for cluster emission, as seen in the top panels of Figure 5.5.

As discussed in Chapter 2, the collective inertia can also have a large impact on the fission dynamics. Using the UNEDF1_{HFB} functional, we compared our result with the non-perturbative cranking ATDHFB inertia \mathcal{M}^{A} to two other expressions for the inertia which are easier to compute and therefore commonly-used in large-scale calculations: the perturbative ATDHFB inertia \mathcal{M}^{AP} (which appears smoothed-out compared to \mathcal{M}^{A}), and the perturbative GCM inertia \mathcal{M}^{GCM} (which is smooth and also lower in magnitude than \mathcal{M}^{A} or \mathcal{M}^{AP} by roughly a factor of 1.5). The result, shown in the middle panels of Figure 5.5, show that the distribution has shifted slightly, but that \mathcal{M}^{AP} and \mathcal{M}^{GCM} give identical, or nearly-identical results. The smoothness of the perturbative inertias apparently allow fluctuations to drive the system to more extreme fragment configurations. This suggests that the magnitude of the inertia matters less than the topography for computing fission yields (though we note that this would not be true for calculating half-lives, which depend exponentially on the magnitude of the inertia).

We also vary the strength of dissipation tensor by adjusting the parameter η . Our starting point η_0 is taken from [45], where it was obtained by adjusting η to match the experimental fragment distribution of ^{294}Pu . Shown in the bottom panel of Figure 5.5, we find that fluctuations do not affect the peak of the distribution, consistent with the results

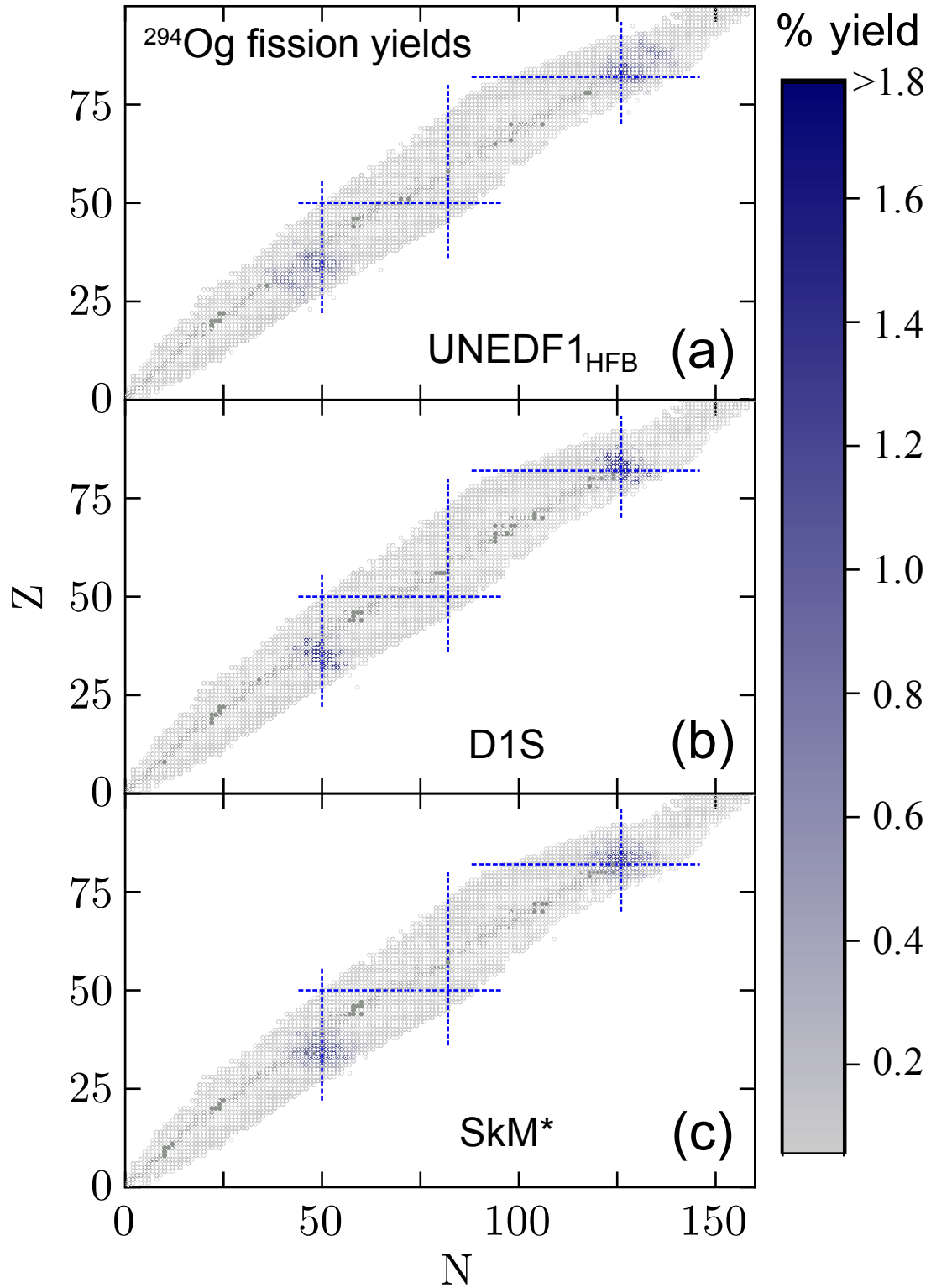


Figure 5.4: Fission fragment distributions for ^{294}Og obtained in UNEDF1_{HFB} (a), D1S (b), and SkM* (c) EDFs using the non-perturbative cranking ATDHFB inertia and the baseline dissipation tensor η_0 . Known isotopes are marked in gray [90]. Magic numbers 50, 82, and 126 are indicated by dotted lines.

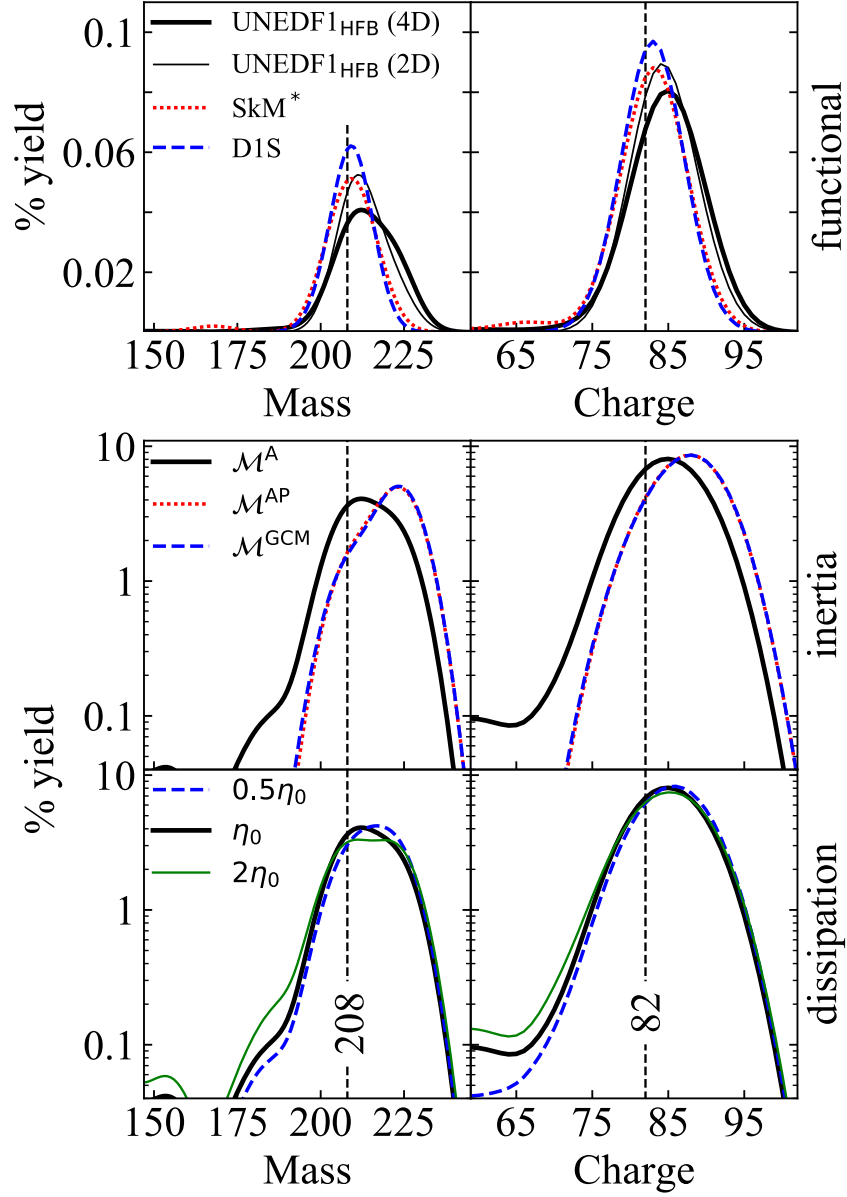


Figure 5.5: Upper panel: Predicted heavy fragment mass (left) and charge (right) yields of ^{294}Og using different functionals (top, linear scale). Bottom panels: collective inertias and dissipation tensor strengths (in logarithmic scale). The baseline calculation was performed using the UNEDF1_{HFB} functional in a 4D space with non-perturbative cranking ATDHFB inertia and dissipation tensor strength η_0 .

of [44, 91, 92]. The primary effect is in the tails.

5.3 Fragment formation in ^{294}Og

The Langevin dynamics approach is useful for calculating fragment yield distributions, but they do not offer much physical insight into the process of fragment formation. In order to better understand fragment formation for the most-probable fragments, we computed the nucleon localization function (section 2.1.3 and References [43, 44]) along the cluster emission path. This is shown in Figure 5.6, where it is compared to the spherical fragments ^{208}Pb and ^{86}Kr . We found that the lead prefragment is well-localized just outside the outer turning line. The $N \approx 50$ neutrons belonging to krypton are also well-localized at early stages of the evolution, but the $Z \approx 36$ protons are not, highlighting the importance of shell closures in prefragment formation.

If this is a general result, one could leverage this insight to predict fission fragments as early as the outer turning line, resulting in a major reduction in total computing time because of the reduced PES. A method which exploits this is described in Appendix A.

5.4 Experimental search for cluster emission in ^{294}Og

The effort to detect cluster emission in SHEs is underway. However, one of the biggest challenges standing in the way of observation of cluster emission from ^{294}Og is the problem of statistics. There have only been 5 recorded instances of ^{294}Og , from the first observations in 2005 [93] to the most recent in 2018 [85].¹ To maximize the possibility of detecting

¹In fact, there were reports as early as 2004 [94] that fission fragments resulting from the spontaneous fission of ^{294}Og may have been detected, but these are unconfirmed.

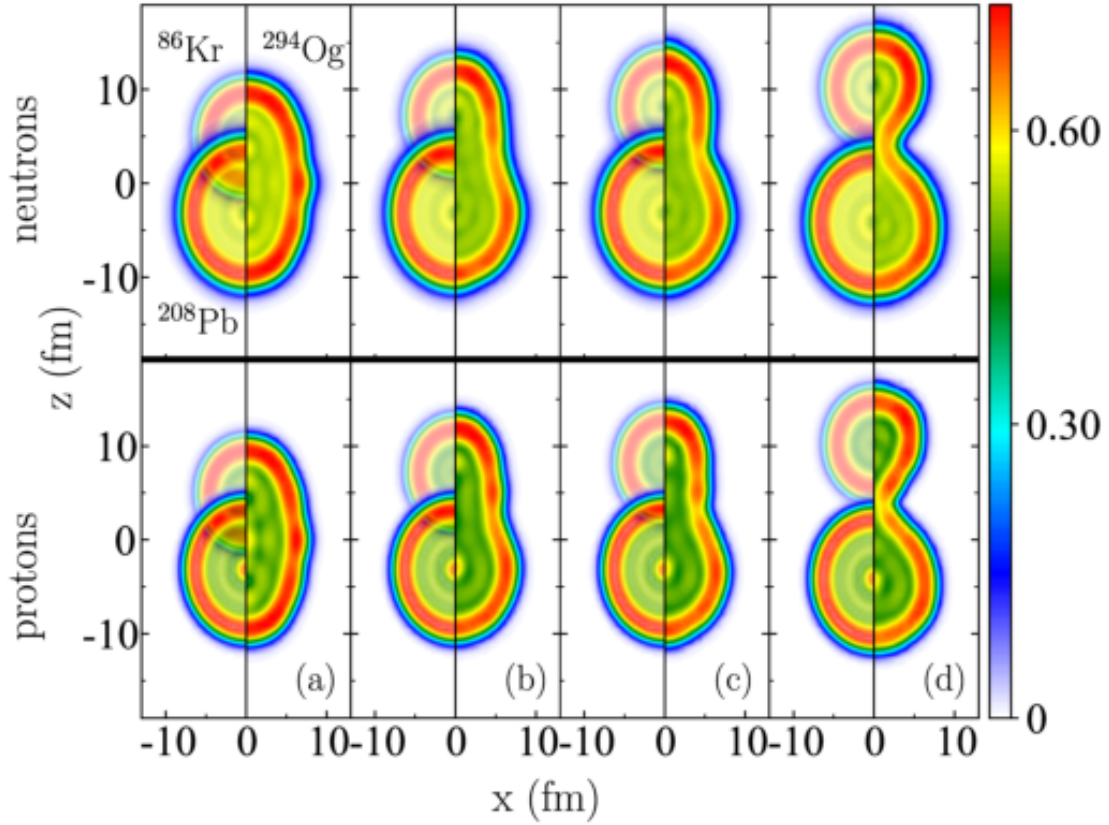


Figure 5.6: Nucleon localization functions for several deformed configurations of ^{294}Og . For comparison, localizations are also shown for the fragments ^{208}Pb and ^{86}Kr on the left side of each subplot. The configurations shown correspond to Fig. 1 from the paper, with multipole moments $(Q_{20}, Q_{30}) =$ (a) $(75 \text{ b}, 0)$; (b) $(120 \text{ b}, 17 \text{ b}^{\frac{3}{2}})$ [$\sim\text{OTL}$]; (c) $(140 \text{ b}, 24 \text{ b}^{\frac{3}{2}})$; and (d) $(264 \text{ b}, 60 \text{ b}^{\frac{3}{2}})$ [$\sim\text{scission}$].

SF events as they happen, there is some discussion in the experimental community about building an ionization chamber with the ability to distinguish fragments by their Z-value. This is discussed at some length in [85]:

“Among these SF events, there were signals correlated with incoming recoil-like signals within the time range of the ^{294}Og half-life. We have inspected the possible assignment of some SF events to the fission of ^{294}Og . In the past, as well very recently, ^{294}Og was considered as a system consisting of doubly magic ^{208}Pb and singly magic $N = 50$, ^{86}Kr . These two components are well bound stable nuclei. One can envision that an asymmetric fission of ^{294}Og into ^{208}Pb and ^{86}Kr fragments might be somewhat enhanced.

“However, especially since the decay time of ^{294}Og is not sufficiently different from ^{258}No decay, one cannot make an assignment to ^{294}Og activity based only on the half-life of SF events. The energy of SF events vary, since we detect sometimes only a partial energy of fission fragments. Such events are more likely to arise from the SF activity produced in a multinucleon transfer involving the Cf isotope in the target. The indistinguishability of complete-fusion from transfer reaction products provides motivation for an ionization chamber, which would have a discrimination capability for the atomic number Z, placed before the implantation Si counter. Construction and anticipated performance of such an ionization chamber based on gas electron multiplier (GEM) technology was recently discussed...”

Chapter 6

Fission in the R Process

6.1 The role of fission in the astrophysical r process

One of the outstanding mysteries in astrophysics is the origin of heavy elements. It is thought that heavy elements are formed in a violent, neutron-heavy astrophysical scenario, such as a supernova or a neutron star merger, as light “seed” nuclei are rapidly bombarded by neutrons. This rapid neutron capture process, generally shortened to “r process,” increases the mass of seed nuclei until eventually they beta decay toward the valley of stability. This process is illustrated schematically in Figure 6.1.

Fission plays an important role in the r process. The competition between neutron capture rates, fission rates, and other decays determines the direction in which the r process proceeds. Fission also places an upper limit on the mass that can be produced in an r-process scenario, as fission lifetimes for heavy and superheavy isotopes become small enough to compete with the neutron flux of the environment around $N \approx 184$. Also, as will be discussed shortly, fissioning isotopes in this mass region are thought to lead to the rare earth peak around $A \approx 165$.

A related topic is the question of fission cycling. Once a heavy nucleus fissions, its fragments can then absorb more neutrons and make their way back up the r-process chain. Elemental abundance patterns in stars outside our solar system somewhat resemble that

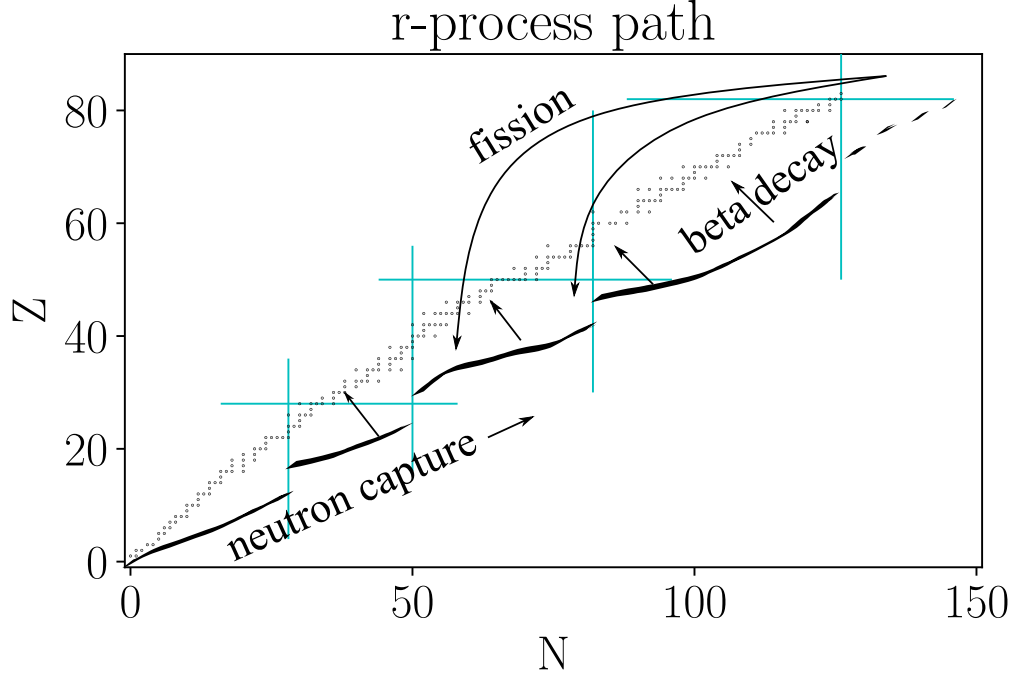


Figure 6.1: Schematic overview of the r process. Neutron capture increases the mass of seed nuclei until they reach the drip line or decay, e.g. via beta decay or fission (spontaneous, beta-delayed, or neutron-induced).

of our own [95], and it has been suggested that fission cycling may be responsible for this “universality” of the r process [96].

R-process network calculations combine nuclear physics inputs, such as decay lifetimes, capture cross sections, and fission fragment yields, with astrophysical inputs, such as temperature and neutron flux, to simulate the complex competition between neutron capture and various forms of nuclear decay. Such calculations require quality inputs from a variety of sources. In order to guide experimental and theoretical efforts and to reduce uncertainties in the abundance pattern, sensitivity studies (in which inputs are tweaked to measure their impact on the final yield) can estimate the impact of a particular set of observables, such as fission fragment yields, on the r-process abundance pattern.

Sensitivity studies indicate that fission yields primarily affect the abundance and location of the rare earth peak and the second r-process peak ($A \approx 100 - 160$) [97, 98]. This can

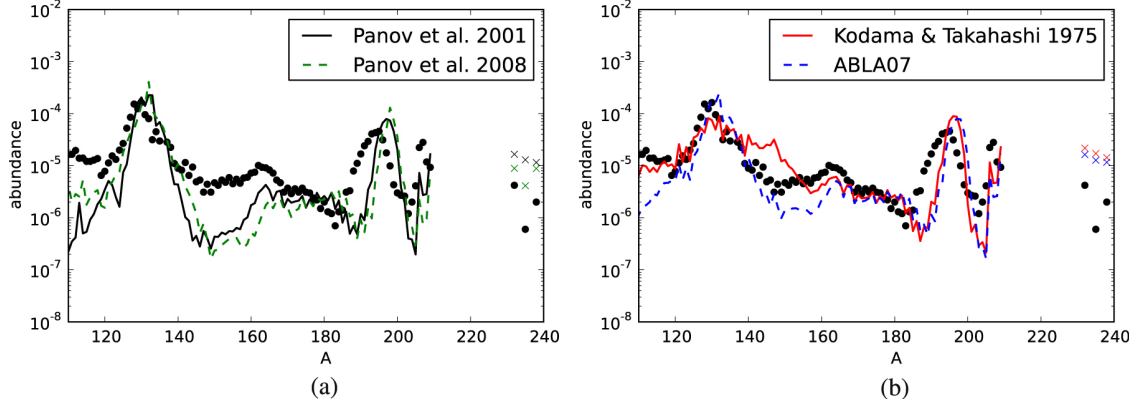


Figure 6.2: Quoting their caption: "Final abundances of the integrated ejecta around the second and third peak for an NSM (Korobkin et al. 2012; Rosswog et al. 2013) at a simulation time $t = 10^6$ s, employing the FRDM mass model combined with four different fission fragment distribution models (see the text). For reasons of clarity the results are presented in two graphs. The abundances for Th and U are indicated by crosses. In the left-hand panel the lower crosses belong to the Panov et al. (2008) model (dashed line), while the lower crosses in the right-hand panel belong to the ABLA07 distribution model (dashed line). The dots represent the solar r-process abundance pattern (Sneden et al. 2008)." [98]

be seen in Figure 6.2, in which four different sets of fission fragment yields were used to compute abundances. That this region should be sensitive to fission yields should come as no great surprise, since most fission fragments are likely to lie in the range $A \approx 100 - 160$.

In [?], the authors performed a sensitivity study in which, instead of assessing uncertainties, their goal was to isolate "hot spots" of nuclei that would have the greatest impact on the final r-process abundances. Four different mass models were used to estimate these hot spots; in Figure 6.3 the neutron-induced fission hot spots are shown, with the four different results superimposed on top of one another. We selected a few of these "hot spot" nuclei to analyze microscopically.

Figure 6.3 shows specifically neutron-induced fission; however, the phenomenological (GEF) yields that were used do not show a strong dependence on excitation energy for many nuclei of interest. Therefore, for simplicity, we simply calculate the spontaneous fission yields. A proper treatment of neutron-induced fission using a finite temperature for-

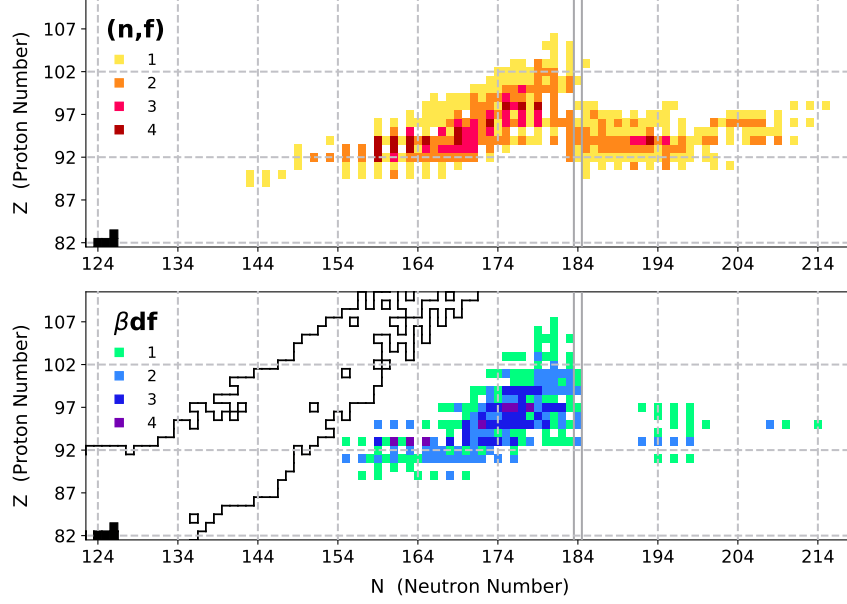


Figure 6.3: Heatmap showing isotopes whose fission yields are especially relevant to the r process. This combines the results from four different mass models, and counts how many mass models found each isotope to be relevant (integrated fission flow above a certain threshold). [?]

malism is being developed [59, 99, 100], but many challenges still remain (see Appendix, \cite{cnr2018-proceedings}).

6.2 Fission fragment yields for r-process nuclei

Using 6.3 as a guide, the isotopes ^{254}Pu , ^{264}Pu , ^{288}Pu , ^{270}Cm , and ^{276}Cf were selected for study. For each isotope, a 1D PES was calculated up to the outermost isomer state by constraining Q_{20} and leaving the other degrees of freedom unconstrained. Between the isomer state and the outer turning line, the PES was expanded to include Q_{30} in order to account for mass asymmetry between the fragments. The WKB method was used to estimate relative probabilities along the outer turning line, at which stage fragment pairs were identified using the localization-based method described in \cite{locali, appendix}.

The resulting distributions will be shown in Figure \ref{???} whenever I have them.

[Maybe the methods portion of this project, and/or the justification of the method, should be moved to another Appendix instead of the main body of the text. It's important, certainly, but it's not central to the narrative]

6.3 Kilonova and ^{254}Cf

An open questions about the r process is where exactly it takes place. Core-collapse supernovae were a leading contender for years, but that hypothesis has recently fallen out of favor because of reasons \cite{???}. Bolstered by theoretical calculations \cite{???} and the neutron star merger event GW170817, neutron star mergers are known to be a source of r-process nuclei; however it is not yet known if neutron star mergers can account for all of the observed r-process abundances [101, 102]. If it turns out that an additional r-process site is needed to explain stellar abundances, another possible location is a collapsar, which has not been observed but which matches the final abundances well in simulations [103, 104]. Regardless, the results are far from conclusive, and stronger evidence is needed. The isotope ^{254}Cf has been identified as a signature to help astronomers identify potential r-process sites.

It is suspected that the kilonova in a neutron star merger is produced by residual radioactivity as neutron-rich material produced in the merger decays toward stability. This material produces an observable light curve, which is one way to characterize the kilonova. The light curve will be dominated by alpha and beta decay events at early times, but if nuclei with spontaneous fission half-lives on the order of several days are produced in sufficient quantities, these would have a major impact on late-time heating in the kilonova, which in turn would affect the light curve. Thus, the shape of the light curve may indicate whether

or not heavy, short-lived actinides were produced.

The question remains whether such nuclei exist which. Limiting ourselves to isotopes which have been experimentally measured, there are several which primarily undergo spontaneous fission and which may be produced in significant quantities in the r process: several isotopes each of californium and fermium, plus ^{260}Md . However, most of the fermium and californium isotopes are too short-lived, and the population of ^{260}Md is highly model-dependent, leaving ^{254}Cf as the most-likely candidate.

Perhaps you should cite [105], if no one else.

The effect of ^{254}Cf on the heating and light curve depends on the energy released during fission, which in turn depends on the fragment yield it produces. Mass and kinetic energy distributions of ^{254}Cf were actually measured in [106]. For some reason, though, Zhu considers that measurement “sparse” and they do some dressing up of it in their paper [105]. We decide to compute it microscopically using our Langevin approach, just to see what useful information we can add.

Chapter 7

Outlook

Having discussed several different results, it is worth taking some time to reflect.

The overarching goal of the project, in which this dissertation is a part, is to describe spontaneous fission observables in a fully self-consistent framework based on fundamental nuclear physics. At this stage, we are able to estimate half-lives and primary fragment distributions [to around X% accuracy, for the nuclei with which comparison to experiment is possible].

7.1 Perspectives for future model development

7.1.1 Numerical challenges

We can hope to achieve greater fidelity in our calculations by

We definitely need a better handle on the inertia. The perturbative inertia is easy to compute, but not terribly reliable. The non-perturbative inertia can certainly do better, but as it is computed now (using finite differences) it is subject to numerical artifacts and instabilities (dependent on the level of convergence of the individual densities, the coefficient multipliers, different basis sizes) as well as to actual physics, such as level crossings which manifest in projections from a higher-dimensional space. One tool that has been suggested which would eliminate the need for finite-difference derivatives is automatic differentiation

\cite{???}.

UNEDF1 seems to underestimate fission barrier heights (artificial though the concept may be; the main impact is probably that lifetimes are underestimated). It also turns out to be a headache to work with, making convergence quite a challenge sometimes (any cases in particular, like for highly-deformed or heavy or octupole-deformed nuclei or something?). Better functionals might hope to better capture the physics, and one can hope they are easier to work with. (here you could mention the DME EDFs; unfortunately, introducing density-dependence causes problems for beyond-mean field corrections)

The construction of a PES is fraught with ambiguities. Trying to reduce a complex system with hundreds of degrees of freedom into only a few collective coordinates creates artificial discontinuities and other artifacts, while at times missing important physics. Brute force computation with a larger number of collective coordinates (such as we did in Chapter 5) will become more accessible as computers continue to become more powerful. However, we might see a faster turnaround on our investment if we start using collective coordinates that better describe the physics of fission. For instance, a set of coordinates D, ξ was proposed as an alternative to the traditional Q_{20}, Q_{30} coordinates in [?], where D is the distance between prefragment centers of mass and $\xi = (A_R - A_L)/A$ characterizes the fragment asymmetry. Using these coordinates, the authors found that they were better able to describe scission configurations than if they had used multipole moments instead.

To that end, it is worth mentioning as well Fragment identification (our localization paper, Marc Verriere's method; you might also mention that this is not an issue in TDDFT, but there you've only got one single fragment pair)

7.1.2 Self-consistent stochastic dynamics

To make the calculations we’ve performed fully self-consistent, we will need to use a microscopic/self-consistent description for dissipation. This is the mechanism which exchanges between intrinsic and collective degrees of freedom, but we handle it in a very ad hoc way with parameters which are fitted instead of determined systematically through some theory. Solving this problem will probably help us with the energetics of fragments (TKE and E^* at the same time!)

A proper understanding of the friction tensor (as it were) may also help with the calculation of neutron emissions, according to this: “The influence of friction on the fission rate was studied in papers [57, 58]. It was shown there that dissipative effects might lead to emission of more neutrons from fissioning nuclei than what is predicted by equilibrium statistical models.” (<https://link.springer.com/article/10.1134%2FS1063779610020012>).

Some other papers you can look at for this might be <https://doi.org/10.1142/S0218301398000105>, <https://doi.org/10.1016/j.physletb.2007.09.072>, and [https://doi.org/10.1016/0375-9474\(79\)00000-0](https://doi.org/10.1016/0375-9474(79)00000-0).

7.2 Perspectives for future physics applications

7.2.1 Half-lives

Although an approach was outlined for computing spontaneous fission half-lives in Chapter 2, no practical results have yet been obtained using this method. The biggest difficulty here is the exponential dependence of the half-life on the action, which is in turn a function of the potential energy, the collective inertia, and the zero-point energy. The numerical improvements outlined above will all serve to ameliorate the situation; additionally, there

are maybe better ways to compute E_0 ? \cite{???}

7.2.2 Collective variables

Experience has shown that the current collective coordinates do not well-describe PESs in the region of ^{178}Pt nor in the r-process region (you can tell because of the sharp cutoffs that indicate scission, and the ridiculously-high saddle points on the neutron-rich side). Better collective coordinates would certainly lead to a better understanding of these nuclei and the way in which they fission. It may also lead to a better understanding of fission overall.

7.2.3 Collective inertia in neutron-deficient sublead region

At the time the ^{180}Hg result was published, microscopic models were not yet sufficiently developed to compute the full fission dynamics. What would the collective energy show? [time-dependent calculations might be interesting to see, as well, but no need to mention that]

7.2.4 Predicting other experimental observables

Furthermore, there are more experimental observables that we should try to predict (refer to Andreyev's review to see what other observables can currently be measured). These include energetics (TKE and E^* , for we have only begun to scratch the surface here), angular momentum, prompt neutron multiplicities (is that within the scope of these self-consistent models?), prompt neutron and gamma energy spectra (getting harder; these are usually handled via statistical models; see intro to [51] for some references), level densities?, and probably more but my mind is blanking. How to compute these in a self-consistent framework

is still an open question. See also the outlook in Nicolas’ review.

Some methods (such as Walid’s, TDDFT, and possibly also this GCM method) are starting to estimate fragment energetics (kinetic and excitation energies). Down the line, there are others who try to predict neutron multiplicities and goodness knows what else using Hauser-Feshbach models and such (FREYA and more). These regions are still disconnected. Of course, these methods still need major refinements in order to better reflect experimental data. Some ideas currently in the pipeline for improving the models are:

7.2.5 Large-scale calculations with machine learning

Something that could be pretty doable and also moderately useful would be to use machine learning for fission yields to use in r-process network calculations. I got this idea from a guy at LLNL who gave a CMSE colloquium. He described a machine learning paradigm (he called it an “Elevated Model”) in which they teach a deep learning network everything it could possibly care to know about a particular model - essentially, creating an emulator of the model. Then you kind of snip off the last couple of layers of your network, and retrain it (holding all but those last two layers constant), this time using experimental data. So by now you’ve gotten most of the physics intuition built into your emulator through the model training, and then for the physical insight your model misses (and perhaps to help reduce overfitting), you’ve taught it where the emulator goes wrong and what to do about it.

How can this help us fission folks? Well, right now the r-process network folks in the FIRE collaboration are using the GEF model for fission fragments and whatnot. It’s basically a black box of magic that is super-overfitted and no one is completely sure how it works. BUT it’s the best they’ve got for fission yields all across the region of interest, so that’s what they use. My thought is to take this as a starting point (our “model data”), and then use

a combination of DFT calculations and also *actual* experimental data as our experimental data. This could be an interesting opportunity to utilize your 290Fm results, along with anything else you've worked on.

Samuel worries (and I think, with justification) that we might not see any substantial improvements because the GEF is already so heavily overfitted. That, and that it might take a really long time (Leo's concerns are similar, plus he is concerned about having enough training data to do anything meaningful). That is why I'm thinking through what would need to be done, step by step, just to get a feel for a timeline of feasibility:

- Finish a 290Fm calculation or something nearby, just to have at least *something* out there
- Figure out how to build a neural network where you can keep some layers fixed while selectively modifying others. I don't think that's something you could do in Scikit-learn; that you'd probably have to build custom (though fortunately you've already got something that might work!). Or you might be able to use TensorFlow (or Keras)
- Determine what observables you'd like (and are able) to include in your evaluation. For sure the locations of the peaks. Maybe also the width? Can you predict a full distribution from the same NN, or do you have to create a different one for each?
- Run the GEF for as many nuclei as you want to include in your evaluation
- Collect theoretical+experimental data you'll use to train your improved model
- Set aside a training set (Ideally you should include something that GEF clearly gets wrong compared to experiment, if possible)

The nice thing about this idea is that it can easily be extended or improved. Maybe some day Peter Moller has calculations across the landscape. You could just swap out the GEF data for Peter Moller's. Basically, it's just glorified interpolation, taking advantage of cheap models and combining/folding those with the more expensive, but more sparse, DFT and experimental results.

However, just based on Figure 1 of [?] and the preliminary yields I have for 266Cm and 290Fm, it doesn't look like we'd be adding too much new information. It looks to me like they already got the basic shape of the yields, and I don't know if I'd do much better with the localization fragment ID approach I'd been considering using.

7.3 Review and conclusions

APPENDICES

Appendix A

Fragment Identification

A.1 Fragments and the nucleon localization function

An improved scission criterion would go beyond simply counting the number of particles in the neck. To help with this, we have a tool at our disposal which helps us to understand correlations that affect fission dynamics. This is called the nucleon localization function, and it allows us to visualize the prefragment nuclear shell structure which largely determines the identity of fission fragments [43].

The nucleon localization function shows that some prefragments can be very well-formed even when the neck is large, while in another case the neck might be small but the prefragments, poorly-defined [44]. A better scission criterion should take into account, or at least be compatible with, the insights gained from the nucleon localization function. As noted in [107], fragment properties on either side of the scission line may differ drastically. This is because shell structure is not well-described geometrically. Our localization measure offers an alternative scheme for identifying fragments before the scission line (see [44]). Since it is based on the underlying quantum shells, it is less sensitive to fluctuations and particle rearrangements late in the evolution.

A.2 The problem of scission

For practical reasons we are limited to describing complicated shapes in terms of just a few parameters, leading to uncertainty in the fragment properties. In particular, the part of the process at which the neck snaps and one nucleus becomes two, called scission, is not well-defined in static approaches.

Many times in static approaches, including the results shown in this dissertation so far, scission is frequently characterized by a single number such as Q_N , which approximately corresponds to the number of particles in the neck. When that number falls below a certain predefined threshold, we say that the nucleus has scissioned. Fragments are identified and one can try to estimate the strength of the repulsive interaction forcing the fragments apart. Of course, as discussed by Younes and Gogny in [28?], wavefunctions corresponding to individual nucleons may extend into the spatial region of the opposite fragment.

This can be understood with an analogy: suppose we stretch a nucleus until a neck forms, and then we use a butcher knife to lop the two fragments apart. This works reasonably well for estimating fragment mass and charge, but it is very poor when it comes to estimating the relative energy of the fragments. To estimate fragment kinetic and excitation energies, one needs to carefully and delicately peel the interlocking fragments apart with a scalpel, or a proper accounting of entanglement and other many-body correlations.

Essentially what we show is that Q_N is meaningless, and that any static definition of scission is going to need to account for the actual configuration of the system.

A.3 Prefragment shell structure

A common theme in all of this has been the importance of the underlying shell structure of the prefragments. Shell energy corrections were found to be important in ^{178}Pt and ^{180}Hg ; cluster formation in ^{294}Og was clearly influenced by the shell structure of the fragments; and the same may or may not be the case for ^{254}Cf . Let's discuss this.

We used localizations to visualize the internal/intrinsic shell structure inside nuclei, and we were able to see that this structure was sometimes intact early in the evolution, at times as far back as the outer turning line. And actually, this kind of makes sense. From just energetics alone, a nucleus on the outer turning line is just as happy (or just as stable, or just as settled) as a nucleus in the ground state. In some sense, it is formed. The difference now is just that the configuration it's in is now unstable due to Coulomb. The two halves, which are kind of maybe happy from a nuclear physics perspective, are pushing apart from the Coulomb repulsion. So that still has to be carried out, but the bulk of the physics might already be done at this point - though not necessarily. It *could* be that the fragments are well-formed and just pushing apart, but that may not be the case. It's like a divorce: sometimes the two have drifted so far apart, or are so well-defined and incompatible as individuals that the divorce is simple and relatively straightforward. Other times, it is a mess trying to sort out who gets what, and the two parties are fundamentally-changed by the proceedings.

I don't have any strong objections to Scamps and Simenel's octupole paper. In fact, to me it kind of makes sense: we've been saying, after all, that it's the shell structure of the deformed prefragments which determine scission, and not necessarily the final fragments themselves. That's really the whole idea behind the localization paper: we're seeing that, at least in some cases, the shell structure is pretty well intact early in the evolution, and that

those prefragments drive the system to scission with some shuffling of the neck nucleons at scission. All they’re saying is that those neck nucleons will affect the shell structure of the prefragments, and just based on the kinds of shapes that the system will take (small neck connecting two elongated or spherical fragments), the prefragments have a strong octupole moment (regardless of whether the fragments are elongated or spherical). So it shouldn’t be the spherical magic numbers we worry about, but the deformed (in this case, octupole-deformed) magic numbers.

I feel like it shouldn’t be too terrible to investigate this claim. What if we constrained the multipole moment(s) that correspond(s) to octupole-deformed fragments (perhaps Q_{50})? I think this parameter might be included in Peter Moller’s model, but not in ours.

A.4 Isospin transport

We’re assuming that the parent nucleus gets to however it gets at the OTL (maybe it just happens to oscillate into that configuration randomly one day, and it feels reasonably stable there (per Witek’s deformed harmonic oscillator paper)), and now we’re trying to argue about how the neck nucleons will flow to rearrange themselves. So we’re already imposing the assumption that the nucleons *will* flow from the neck to the fragments (and indeed, that at least seems to be what happens based on the success of this type of model so far).

This is indeed in contradiction with Scamps and Simenel’s paper, because they essentially claim that once you get to that OTL configuration, the octupole deformation of the fragments (created by a spherical-ish prefragment with neck nucleons on the side, giving it a non-zero Q_{30}) is sufficiently strong to snap the neck and let the fragments go on their merry way, octupole-deformed and everything. On the other hand, we’re saying that instead, it’s

just a lucky coincidence that the fragments are stable in an octupole-deformed configuration because they're not going to stay that way once the neck nucleons flow to their final destination.

There are these isospin transport papers essentially describe the flow of isospin and density in terms of the chemical potential and gradients. Nucleons will flow based on the chemical potential* properties of the system, or in other words, to minimize the binding energy of the system. In general, that means you'll see a flow of neck nucleons in such a way as to bring the final fragments as [jointly] close to stability as possible.

* Reminder on chemical potential: $\mu \equiv \left(\frac{\partial U}{\partial N} \right)_{S,V}$, or essentially the energy per particle which is added/removed from the system. μ must be negative for bosons (else the grand canonical potential will be an exponentially-increasing function), but it can be positive or negative for fermions

The density gradient terms will lead to a flow of nucleons from prefragments to neck (with apparently a greater effect on neutrons than on protons).

Jhila sent a couple of experimental papers where alpha clusters were observed emitting from the neck (perpendicular to the momenta of the fragments). Might this localization tool be used to later help model neutron and alpha emission?

Appendix B

Temperature-Dependent ATDHFB Collective Inertia

B.1 Fission at finite temperature

Everything which was shown in this dissertation assumed that the system was maintained at temperature $T = 0$ and the nucleus behaved as a superfluid below the Fermi surface. However, in many environments (such as a neutron star merger or a nuclear blast) there may be quite a bit of excitation energy imparted to the system, which would raise the temperature above the Fermi surface. Additionally, and more relevant to this dissertation, a finite-temperature formalism is used to describe neutron-induced fission in, e.g. [59]. In the $T \neq 0$ case, pairs may be broken and various excited states are accessible, resulting in changes to the the potential energy surface and, as will be shown in this chapter, the collective inertia.

A lot of these ideas I'm getting from [100] as well as Nicolas' own temperature-dependent HFB notes.

B.2 Finite-temperature density

As in any statistical theory, one first must determine which sort of ensemble properly describes the system. Nuclei are systems which have a conserved number of particles; however, HFB theory explicitly breaks particle number symmetry because of the Bogoliubov transformation. In principle we should perhaps use a microcanonical ensemble to describe a nucleus as a closed, isolated system, but that turns out to be challenging to solve because it requires a full knowledge of the eigenspectrum of the nucleus. Using the particle non-conserving quirk of HFB theory, we wiggle our way out of this hairiness¹ to instead describe our system using the grand canonical ensemble, and this approach turns out to be tractable.

Moving forward by minimizing the grand potential Ω gives us for the density:

$$\hat{D} = \frac{1}{Z} e^{-\beta(\hat{H} - \mu\hat{N})} \quad (\text{B.1})$$

with associated partition function

$$Z = \text{Tr} \left[e^{-\beta(\hat{H} - \mu\hat{N})} \right] \quad (\text{B.2})$$

Moving toward our particular choice of mean-field Hamiltonian, we substitute some one-body operator for the exponent:

$$\hat{D}_{HF} = \frac{1}{Z} e^{-\beta\hat{K}}, Z = \text{Tr} \left[e^{-\beta\hat{K}} \right] \quad (\text{B.3})$$

where in the simple Hartree-Fock case, $\hat{K} = \sum_{ij} K_{ij} c_i^\dagger c_j$ (in the HFB case, \hat{K} is a sum of

¹You can wave your hands here and say that finite temperatures let you break superfluid pairs, and so the number of “quasiparticles” (which, you could argue, might have referred to pairs previously but might now be extended to also include individual, unpaired particles) can change.

all different one-body operator types, but it's the same basic idea).

Defining the HF density matrix $\rho_{ij} = Tr \left[\hat{D}_{HF} c_j^\dagger c_i \right]$, we can show the following useful correspondence relations:

$$\rho = \frac{1}{1 + e^{\beta \hat{K}}} \quad (\text{B.4})$$

$$Tr \left[\hat{D}_{HF} \hat{A} \right] = tr \left[\rho \hat{A} \right] = \sum_{ij} \rho_{ij} \hat{A}_{ij} \quad (\text{B.5})$$

where \hat{A} is an arbitrary operator in the single-particle basis. Similar things happen for the HFB case. At the end of the day in HFB, things work out to be pretty similar to the way they were before (see the full derivation in [108]), except the density in the quasiparticle basis is replaced by

$$\mathcal{R} = \begin{pmatrix} 0 & 0 \\ 0 & 1 \end{pmatrix} \rightarrow \begin{pmatrix} f & 0 \\ 0 & 1 - f \end{pmatrix} \quad (\text{B.6})$$

with the Fermi factor f given by $f_\mu = \frac{1}{1 + e^{\beta E_\mu}}$.

B.3 Temperature-dependent ATDHFB

Let us quickly review the essence of Time-Dependent Hartree-Fock-Bogoliubov (TDHFB). The fundamental assumption of TDHFB is that a system which is a Slater determinant at time $t = 0$ and which is then allowed to evolve in time will remain a Slater determinant at all times t . This assumption allows us to write to TDHFB equation:

$$i\hbar\dot{\mathcal{R}} = [\mathcal{H}, \mathcal{R}] \quad (\text{B.7})$$

where in the single-particle basis

$$\tilde{\mathcal{H}} = \begin{pmatrix} h - \lambda & \Delta \\ -\Delta^* & -h^* + \lambda \end{pmatrix}, \quad \tilde{\mathcal{R}} = \begin{pmatrix} \rho & \kappa \\ -\kappa^* & 1 - \rho^* \end{pmatrix} \quad (\text{B.8})$$

The *additional* assumption that collective motion is slow compared to single particle motion of the system is called the *adiabtic approximation*, and the consequent model is called Adiabatic Time-Dependent Hartree-Fock-Bogoliubov (ATDHFB). Historically, the reason for this assumption comes from microscopic-macroscopic models of nuclear fission, where the dynamics of the system are described by a few collective shape variables and their derivatives (analogous to coordinates and velocities). The adiabatic approximation is implicit in this assumption. ATDHFB provides the bridge for bringing this useful framework into a self-consistent, fully-microscopic picture.

Once the system is described in terms of collective coordinates and velocities, the energy can be expressed as the sum of a “potential” term (which depends on the coordinates) and a “kinetic” term (which depends on the velocities). Our goal is to understand the kinetic part of the energy, which in some sense describes the dynamics of a deformed nucleus, in terms of the first few multipole moments of the nucleus. A key component of this will be the inertia tensor \mathcal{M} , which plays the role of the “mass”: $E_{kin} \sim \frac{1}{2}\mathcal{M}\dot{q}^2$

B.3.1 Review of ATDHFB

With the adiabatic assumption in place, we can write the density as an expansion around some time-even zeroth-order density:

$$\mathcal{R}(t) = e^{i\chi(t)}\mathcal{R}_0(t)e^{-i\chi(t)} \quad (\text{B.9})$$

$$= \mathcal{R}_0 + \mathcal{R}_1 + \mathcal{R}_2 + \dots \quad (\text{B.10})$$

where χ is assumed to be “small” (which is explained more rigorously in [109]) and

$$\mathcal{R}_1 = i[\chi, \mathcal{R}_0] \quad (\text{B.11})$$

$$\mathcal{R}_2 = \frac{1}{2}[[\chi, \mathcal{R}_0], \chi] \quad (\text{B.12})$$

The HFB matrix, being a function of \mathcal{R} , is likewise expanded:

$$\mathcal{H} = \mathcal{H}_0 + \mathcal{H}_1 + \mathcal{H}_2 + \dots \quad (\text{B.13})$$

and together \mathcal{R} and \mathcal{H} are plugged into the TDHFB equation B.7. Gathering terms in powers of χ :

$$i\hbar\dot{\mathcal{R}}_0 = [\mathcal{H}_0, \mathcal{R}_1] + [\mathcal{H}_1, \mathcal{R}_0] \quad (\text{B.14})$$

$$i\hbar\dot{\mathcal{R}}_1 = [\mathcal{H}_0, \mathcal{R}_0] + [\mathcal{H}_0, \mathcal{R}_2] + [\mathcal{H}_1, \mathcal{R}_1] + [\mathcal{H}_2, \mathcal{R}_0] \quad (\text{B.15})$$

These two equations are the ATDHFB equations. They can be solved self-consistently to find both χ and \mathcal{R}_0 ; however, this is rarely done in practice. A more common trick is to exploit the fact that solutions to the ATDHFB equations are (by design) *close* to true HFB solutions. One can then take an HFB solution and compute its time derivative by the first ATDHFB equation B.14 to get ATDHFB-like behavior without going through the full trouble of ATDHFB.

One nice feature of using true HFB solutions instead of ATDHFB solutions is that the matrix \mathcal{H}_0 is diagonal in the HFB basis.

Finally, the total energy of the system is found to be

$$E(\mathcal{R}) = E_{HFB} + \frac{1}{2}\text{Tr}(\mathcal{H}_0\mathcal{R}_1) + \frac{1}{2}\text{Tr}(\mathcal{H}_0\mathcal{R}_2) + \frac{1}{4}\text{Tr}(\mathcal{H}_1\mathcal{R}_1) \quad (\text{B.16})$$

The “kinetic energy” of the system is given by the latter two terms, which (as we’ll show explicitly in a moment), are both second order in χ .

B.3.2 Relation between χ and $\dot{\mathcal{R}}$

Eventually we’ll want to express the energy in terms of the multipole moments q and their derivatives, but for now we will content ourselves with expressing the energy in terms of \mathcal{R} and $\dot{\mathcal{R}}$.

Working in the HFB quasiparticle basis, we have (at finite temperatures)

$$\mathcal{H}_0 = \begin{pmatrix} E & 0 \\ 0 & -E \end{pmatrix}, \quad \mathcal{R}_0 = \begin{pmatrix} f & 0 \\ 0 & 1 - f \end{pmatrix} \quad (\text{B.17})$$

Note that the block matrices E and f are both diagonal. In this same basis, we can also

divide the perturbation matrix χ and the first-order energy \mathcal{H}_1 in the same block matrix form:

$$\chi = \begin{pmatrix} \chi^{11} & \chi^{12} \\ \chi^{21} & \chi^{22} \end{pmatrix}, \quad \mathcal{H}_1 = \begin{pmatrix} \mathcal{H}_1^{11} & \mathcal{H}_1^{12} \\ \mathcal{H}_1^{21} & \mathcal{H}_1^{22} \end{pmatrix} \quad (\text{B.18})$$

Ultimately, by combining these with equations B.11, B.12, and B.14, we arrive at the result:

$$\begin{aligned} \hbar \dot{\mathcal{R}}_{(0),ab}^{11} &= (E_a - E_b)(f_b - f_a)\chi_{ab}^{11} + (f_b - f_a)\mathcal{H}_{(1),ab}^{11} \\ \hbar \dot{\mathcal{R}}_{(0),ab}^{12} &= (E_a + E_b)(1 - (f_a + f_b))\chi_{ab}^{12} + (1 - (f_a + f_b))\mathcal{H}_{(1),ab}^{12} \\ \hbar \dot{\mathcal{R}}_{(0),ab}^{21} &= (E_a + E_b)(1 - (f_a + f_b))\chi_{ab}^{21} - (1 - (f_a + f_b))\mathcal{H}_{(1),ab}^{21} \\ \hbar \dot{\mathcal{R}}_{(0),ab}^{22} &= (E_a - E_b)(f_b - f_a)\chi_{ab}^{22} - (f_b - f_a)\mathcal{H}_{(1),ab}^{22} \end{aligned} \quad (\text{B.19})$$

It is common (the so-called “cranking approximation”) to assume that changes in the density have approximately no effect on the mean field, in which case these relations reduce to

$$\begin{aligned} \hbar \dot{\mathcal{R}}_{(0),ab}^{11} &= (E_a - E_b)(f_b - f_a)\chi_{ab}^{11} \\ \hbar \dot{\mathcal{R}}_{(0),ab}^{12} &= (E_a + E_b)(1 - (f_a + f_b))\chi_{ab}^{12} \\ \hbar \dot{\mathcal{R}}_{(0),ab}^{21} &= (E_a + E_b)(1 - (f_a + f_b))\chi_{ab}^{21} \\ \hbar \dot{\mathcal{R}}_{(0),ab}^{22} &= (E_a - E_b)(f_b - f_a)\chi_{ab}^{22} \end{aligned} \quad (\text{B.20})$$

Sanity Check: In the $T = f = 0$ case, the 11 and 22 terms vanish completely and we are left with the familiar [zero-temperature] ATDHFB equations:

$$\hbar \dot{\mathcal{R}}_{(0),ab}^{12} = (E_a + E_b) \chi_{ab}^{12} + \mathcal{H}_{(1),ab}^{12} \quad (\text{B.21})$$

$$\hbar \dot{\mathcal{R}}_{(0),ab}^{21} = (E_a + E_b) \chi_{ab}^{21} - \mathcal{H}_{(1),ab}^{21} \quad (\text{B.22})$$

Another thing we must be careful of is the case of degenerate states. In such an event, $E_a = E_b$ and $f_a = f_b$, leading again to $\dot{\mathcal{R}}_{(0),ab}^{11} = \dot{\mathcal{R}}_{(0),ab}^{22} = 0$ (but I emphasize that this is only for this particular pair of states $|a\rangle$ and $|b\rangle$).

A third, rather pedantic case to be aware of is the example of a two-state system. In that case, $f_a + f_b = 1$ and then the opposite happens; namely, $\dot{\mathcal{R}}_{(0),ab}^{12} = \dot{\mathcal{R}}_{(0),ab}^{21} = 0$ while $\dot{\mathcal{R}}_{(0),ab}^{11} \neq 0, \dot{\mathcal{R}}_{(0),ab}^{22} \neq 0$

B.3.3 Kinetic energy at finite temperature

As mentioned previously, the expression for the “kinetic” energy of the system is given by:

$$E_{kin}(\mathcal{R}) = \frac{1}{2} \text{Tr}(\mathcal{H}_0 \mathcal{R}_2) + \frac{1}{4} \text{Tr}(\mathcal{H}_1 \mathcal{R}_1) \quad (\text{B.23})$$

B.3.3.1 Term proportional to \mathcal{R}_2

It can be shown that

$$\text{Tr}(\mathcal{H}_0 \mathcal{R}_2) = \frac{1}{2} \text{Tr}([\chi, \mathcal{H}_0] [\chi, \mathcal{R}_0]) \quad (\text{B.24})$$

which leads to

$$[\chi, \mathcal{H}_0] = \begin{pmatrix} [\chi^{11}, E] & -\{\chi^{12}, E\} \\ \{\chi^{21}, E\} & -[\chi^{22}, E] \end{pmatrix}, \quad [\chi, \mathcal{R}_0] = \begin{pmatrix} [\chi^{11}, f] & \chi^{12} - \{\chi^{12}, f\} \\ -\chi^{21} + \{\chi^{21}, f\} & -[\chi^{22}, f] \end{pmatrix} \quad (\text{B.25})$$

$$\begin{aligned} \text{Tr}(\mathcal{H}_0 \mathcal{R}_2) = \frac{1}{2} \text{Tr} & \left([\chi^{11}, E][\chi^{11}, f] + \{\chi^{12}, E\}(\chi^{21} - \{\chi^{21}, f\}) \right. \\ & \left. + \{\chi^{21}, E\}(\chi^{12} - \{\chi^{12}, f\}) + [\chi^{22}, E][\chi^{22}, f] \right) \end{aligned} \quad (\text{B.26})$$

Since E and f are diagonal, we can simplify expressions involving commutators and anticommutators. If A is an arbitrary matrix and D is diagonal, then

$$[A, D]_{\mu\nu} = (D_\nu - D_\mu)A_{\mu\nu} \quad (\text{B.27})$$

$$\{A, D\}_{\mu\nu} = (D_\mu + D_\nu)A_{\mu\nu} \quad (\text{B.28})$$

$$A_{\mu\nu} - \{A, D\}_{\mu\nu} = (1 - D_\mu - D_\nu)A_{\mu\nu} \quad (\text{B.29})$$

Then this energy term becomes

$$\frac{1}{2} \text{Tr}(\mathcal{H}_0 \mathcal{R}_2) = \frac{1}{4} \left[(E_b - E_a)(f_a - f_b)\chi_{ab}^{11}\chi_{ba}^{11} + (E_a + E_b)(1 - f_a - f_b)\chi_{ab}^{12}\chi_{ba}^{21} \right. \quad (\text{B.30})$$

$$\left. + (E_a + E_b)(1 - f_a - f_b)\chi_{ab}^{21}\chi_{ba}^{12} + (E_b - E_a)(f_a - f_b)\chi_{ab}^{22}\chi_{ba}^{22} \right] \quad (\text{B.31})$$

If you wanted to get *really* crazy (and we'll see in a bit why this might actually be okay), you could even throw in some extra delta functions to get this:

$$\frac{1}{2}\text{Tr}(\mathcal{H}_0\mathcal{R}_2) = \frac{1}{4} \left[(E_b - E_a)(f_a - f_b)\delta_{a\alpha}\delta_{b\beta}\chi_{\alpha\beta}^{11}\chi_{ba}^{11} + (E_a + E_b)(1 - f_a - f_b)\delta_{a\alpha}\delta_{b\beta}\chi_{\alpha\beta}^{12}\chi_{ba}^{21} \right. \\ \left. + (E_a + E_b)(1 - f_a - f_b)\delta_{a\alpha}\delta_{b\beta}\chi_{\alpha\beta}^{21}\chi_{ba}^{12} + (E_b - E_a)(f_a - f_b)\delta_{a\alpha}\delta_{b\beta}\chi_{\alpha\beta}^{22}\chi_{ba}^{22} \right] \quad (\text{B.32})$$

$$+ (E_a + E_b)(1 - f_a - f_b)\delta_{a\alpha}\delta_{b\beta}\chi_{\alpha\beta}^{21}\chi_{ba}^{12} + (E_b - E_a)(f_a - f_b)\delta_{a\alpha}\delta_{b\beta}\chi_{\alpha\beta}^{22}\chi_{ba}^{22} \quad (\text{B.33})$$

Note that this now has the general form

$$\frac{1}{2}\text{Tr}(\mathcal{H}_0\mathcal{R}_2) = \bar{\mathcal{M}}'^{11,11}_{\alpha\beta ab}\chi_{\alpha\beta}^{11}\chi_{ba}^{11} + \bar{\mathcal{M}}'^{12,21}_{\alpha\beta ab}\chi_{\alpha\beta}^{12}\chi_{ba}^{21} + \bar{\mathcal{M}}'^{21,12}_{\alpha\beta ab}\chi_{\alpha\beta}^{21}\chi_{ba}^{12} + \bar{\mathcal{M}}'^{22,22}_{\alpha\beta ab}\chi_{\alpha\beta}^{22}\chi_{ba}^{22} \quad (\text{B.34})$$

where everything that isn't a χ has been absorbed into a single coefficient.

Pausing for a moment to reflect on what has just happened: Remember that the goal all along has been to treat this piece of the energy as sort of a “kinetic energy term” describing motion in a space of collective shape deformation coordinates. Then just now we found that, sure enough, we can factor this particular chunk into something that looks *kind of* like $\frac{1}{2}mv^2$. And we already know from B.20 that χ is related to $\dot{\mathcal{R}}_0$. Eventually we'll try to relate $\dot{\mathcal{R}}_0$ to the collective shape coordinates \dot{q} , but first let's see if we can't get the other piece of the kinetic energy into the same form.

B.3.3.2 Term proportional to \mathcal{R}_1

Recall that $\mathcal{R}_1 = i[\chi, \mathcal{R}_0]$; then we can almost copy from equation B.26 of the previous section:

$$\begin{aligned}
\frac{1}{4}\text{Tr}(\mathcal{H}_1\mathcal{R}_1) &= \frac{i}{4}\text{Tr}\left(\mathcal{H}_1^{11}[\chi^{11}, f] - \mathcal{H}_1^{12}(\chi^{21} - \{\chi^{21}, f\}) \right. \\
&\quad \left. + \mathcal{H}_1^{21}(\chi^{12} - \{\chi^{12}, f\}) - \mathcal{H}_1^{22}[\chi^{22}, f]\right) \\
&= \frac{i}{4}\left(\mathcal{H}_{(1),ab}^{11}(f_a - f_b)\chi_{ba}^{11} - \mathcal{H}_{(1),ab}^{12}(1 - f_a - f_b)\chi_{ba}^{21} \right. \\
&\quad \left. + \mathcal{H}_{(1),ab}^{21}(1 - f_a - f_b)\chi_{ba}^{12} - \mathcal{H}_{(1),ab}^{22}(f_a - f_b)\chi_{ba}^{22}\right) \quad (\text{B.35})
\end{aligned}$$

But what are those \mathcal{H}^1 terms? Since the interaction is known in the single-particle basis, we'll have to transform our density into the single-particle basis $\mathcal{R}_1 \rightarrow \tilde{\mathcal{R}}_1$, evaluate $\tilde{\mathcal{H}}_1$ (which depends on $\tilde{\mathcal{R}}_1$) in this basis, and then transform the result back into the quasiparticle basis $\tilde{\mathcal{H}}_1 \rightarrow \mathcal{H}_1$

$$\tilde{\mathcal{R}}_1 = \begin{pmatrix} \rho_1 & \kappa_1 \\ -\kappa_1^* & -\rho_1^* \end{pmatrix} = i \begin{pmatrix} U & V^* \\ V & U^* \end{pmatrix} \begin{pmatrix} [\chi^{11}, f] & \chi^{12} - \{\chi^{12}, f\} \\ -\chi^{21} + \{\chi^{21}, f\} & -[\chi^{22}, f] \end{pmatrix} \begin{pmatrix} U^\dagger & V^\dagger \\ V^T & U^T \end{pmatrix} \quad (\text{B.36})$$

$$\Rightarrow \rho_1 = i \left(U[\chi^{11}, f]U^\dagger + U \left(\chi^{12} - \{\chi^{12}, f\} \right) V^T - V^* \left(\chi^{21} - \{\chi^{21}, f\} \right) U^\dagger - V^*[\chi^{22}, f]V^T \right) \quad (\text{B.37})$$

$$\kappa_1 = i \left(U[\chi^{11}, f]V^\dagger + U \left(\chi^{12} - \{\chi^{12}, f\} \right) U^T - V^* \left(\chi^{21} - \{\chi^{21}, f\} \right) V^\dagger - V^*[\chi^{22}, f]U^T \right) \quad (\text{B.38})$$

In the single-particle basis, we can compute the interaction mean field $\Gamma_{(1),ij} = \bar{V}_{ijkl}\rho_{(1),lk}$ and the pairing field $\Delta_{(1),ij} = \frac{1}{2}\bar{V}_{ijkl}\kappa_{(1),kl}$:

$$\Gamma_{(1),ij} = \bar{v}_{ikjl}\rho_{(1),lk} \quad (\text{B.39})$$

$$= i\bar{v}_{ikjl} \left(U_{l\alpha}[\chi^{11}, f]_{\alpha\beta} U_{\beta k}^\dagger + U_{l\alpha} \left(\chi^{12} - \left\{ \chi^{12}, f \right\} \right)_{\alpha\beta} V_{\beta k}^T \right. \quad (\text{B.40})$$

$$\left. - V_{l\alpha}^* \left(\chi^{21} - \left\{ \chi^{21}, f \right\} \right)_{\alpha\beta} U_{\beta k}^\dagger - V_{l\alpha}^*[\chi^{22}, f]_{\alpha\beta} V_{\beta k}^T \right) \quad (\text{B.41})$$

$$\Delta_{(1),ij} = \frac{1}{2} \bar{v}_{ijkl} \kappa_{(1),kl} \quad (\text{B.42})$$

$$= \frac{i}{2} \bar{v}_{ijkl} \left(U_{l\alpha}[\chi^{11}, f]_{\alpha\beta} V_{\beta k}^\dagger + U_{l\alpha} \left(\chi^{12} - \left\{ \chi^{12}, f \right\} \right)_{\alpha\beta} U_{\beta k}^T \right. \quad (\text{B.43})$$

$$\left. - V_{l\alpha}^* \left(\chi^{21} - \left\{ \chi^{21}, f \right\} \right)_{\alpha\beta} V_{\beta k}^\dagger - V_{l\alpha}^*[\chi^{22}, f]_{\alpha\beta} U_{\beta k}^T \right) \quad (\text{B.44})$$

To clean up the presentation a bit, let us introduce the following:

$$J_{ij\alpha\beta}^{11} = i\bar{v}_{ikjl} U_{l\alpha} U_{\beta k}^\dagger \quad J_{ij\alpha\beta}^{22} = -i\bar{v}_{ikjl} V_{l\alpha}^* V_{\beta k}^T \quad (\text{B.45})$$

$$K_{ij\alpha\beta}^{12} = i\bar{v}_{ikjl} U_{l\alpha} V_{\beta k}^T \quad K_{ij\alpha\beta}^{21} = -i\bar{v}_{ikjl} V_{l\alpha}^* U_{\beta k}^\dagger \quad (\text{B.46})$$

$$L_{ij\alpha\beta}^{12} = i\bar{v}_{ijkl} U_{l\alpha} U_{\beta k}^T \quad L_{ij\alpha\beta}^{21} = -i\bar{v}_{ijkl} V_{l\alpha}^* V_{\beta k}^\dagger \quad (\text{B.47})$$

$$M_{ij\alpha\beta}^{11} = i\bar{v}_{ijkl} U_{l\alpha} V_{\beta k}^\dagger \quad M_{ij\alpha\beta}^{22} = -i\bar{v}_{ijkl} V_{l\alpha}^* U_{\beta k}^T \quad (\text{B.48})$$

Then the fields simplify to

$$\Gamma_{(1),ij} = J_{ij\alpha\beta}^{11}[\chi^{11}, f]_{\alpha\beta} + K_{ij\alpha\beta}^{12}\left(\chi^{12} - \{\chi^{12}, f\}\right)_{\alpha\beta} + K_{ij\alpha\beta}^{12}\left(\chi^{21} - \{\chi^{21}, f\}\right)_{\alpha\beta} + J_{ij\alpha\beta}^{22}[\chi^{22}, f]_{\alpha\beta} \quad (\text{B.49})$$

$$2\Delta_{(1),ij} = M_{ij\alpha\beta}^{11}[\chi^{11}, f]_{\alpha\beta} + L_{ij\alpha\beta}^{12}\left(\chi^{12} - \{\chi^{12}, f\}\right)_{\alpha\beta} + L_{ij\alpha\beta}^{12}\left(\chi^{21} - \{\chi^{21}, f\}\right)_{\alpha\beta} + M_{ij\alpha\beta}^{22}[\chi^{22}, f]_{\alpha\beta} \quad (\text{B.50})$$

Now we can transform the fields back into the quasiparticle basis:

$$\mathcal{H}_1 = \begin{pmatrix} U^\dagger & V^\dagger \\ V^T & U^T \end{pmatrix} \begin{pmatrix} \Gamma_1 & \Delta_1 \\ -\Delta_1^* & -\Gamma_1^* \end{pmatrix} \begin{pmatrix} U & V^* \\ V & U^* \end{pmatrix} \quad (\text{B.51})$$

$$= \begin{pmatrix} U^\dagger\Gamma_1U + U^\dagger\Delta_1V - V^\dagger\Delta_1^*U - V^\dagger\Gamma_1^*V & U^\dagger\Gamma_1V^* + U^\dagger\Delta_1U^* - V^\dagger\Delta_1^*V^* - V^\dagger\Gamma_1^*U^* \\ V^T\Gamma_1U + V^T\Delta_1V - U^T\Delta_1^*U - U^T\Gamma_1^*V & V^T\Gamma_1V^* + V^T\Delta_1U^* - U^T\Delta_1^*V^* - U^T\Gamma_1^*U^* \end{pmatrix} \quad (\text{B.52})$$

Assuming further that the full matrix χ is Hermitian, then $\chi^{11*} = \chi^{11}$, $\chi^{22*} = \chi^{22}$, and $\chi^{12*} = \chi^{21}$. This leads in turn to

$$[\chi^{11}, f]^* = -[\chi^{11}, f] \quad (\text{B.53})$$

$$[\chi^{22}, f]^* = -[\chi^{22}, f] \quad (\text{B.54})$$

$$\left(\chi^{12} - \{\chi^{12}, f\}\right)^* = \left(\chi^{21} - \{\chi^{21}, f\}\right) \quad (\text{B.55})$$

$$\left(\chi^{21} - \{\chi^{21}, f\}\right)^* = \left(\chi^{12} - \{\chi^{12}, f\}\right) \quad (\text{B.56})$$

The whole thing written out is

$$\mathcal{H}_{(1),ab}^{11} = \left(U_{ai}^\dagger U_{jb} J_{ij\alpha\beta}^{11} + U_{ai}^\dagger V_{jb} \frac{M_{ij\alpha\beta}^{11}}{2} + V_{ai}^\dagger U_{jb} \frac{M_{ij\alpha\beta}^{11*}}{2} + V_{ai}^\dagger V_{jb} J_{ij\alpha\beta}^{11*} \right) (f_\beta - f_\alpha) \chi_{\alpha\beta}^{11} \quad (\text{B.57})$$

$$+ \left(U_{ai}^\dagger U_{jb} J_{ij\alpha\beta}^{22} + U_{ai}^\dagger V_{jb} \frac{M_{ij\alpha\beta}^{22}}{2} + V_{ai}^\dagger U_{jb} \frac{M_{ij\alpha\beta}^{22*}}{2} + V_{ai}^\dagger V_{jb} J_{ij\alpha\beta}^{22*} \right) (f_\beta - f_\alpha) \chi_{\alpha\beta}^{22} \quad (\text{B.58})$$

$$+ \left(U_{ai}^\dagger U_{jb} K_{ij\alpha\beta}^{12} + U_{ai}^\dagger V_{jb} \frac{L_{ij\alpha\beta}^{12}}{2} - V_{ai}^\dagger U_{jb} \frac{L_{ij\alpha\beta}^{21*}}{2} + V_{ai}^\dagger V_{jb} K_{ij\alpha\beta}^{21*} \right) (1 - f_\alpha - f_\beta) \chi_{\alpha\beta}^{12} \quad (\text{B.59})$$

$$+ \left(U_{ai}^\dagger U_{jb} K_{ij\alpha\beta}^{21} + U_{ai}^\dagger V_{jb} \frac{L_{ij\alpha\beta}^{21}}{2} - V_{ai}^\dagger U_{jb} \frac{L_{ij\alpha\beta}^{12*}}{2} + V_{ai}^\dagger V_{jb} K_{ij\alpha\beta}^{12*} \right) (1 - f_\alpha - f_\beta) \chi_{\alpha\beta}^{21} \quad (\text{B.60})$$

$$\mathcal{H}_{(1),ab}^{12} = \left(U_{ai}^\dagger V_{jb}^* J_{ij\alpha\beta}^{11} + U_{ai}^\dagger U_{jb}^* \frac{M_{ij\alpha\beta}^{11}}{2} + V_{ai}^\dagger V_{jb}^* \frac{M_{ij\alpha\beta}^{11*}}{2} + V_{ai}^\dagger U_{jb}^* J_{ij\alpha\beta}^{11*} \right) (f_\beta - f_\alpha) \chi_{\alpha\beta}^{11} \quad (\text{B.61})$$

$$+ \left(U_{ai}^\dagger V_{jb}^* J_{ij\alpha\beta}^{22} + U_{ai}^\dagger U_{jb}^* \frac{M_{ij\alpha\beta}^{22}}{2} + V_{ai}^\dagger V_{jb}^* \frac{M_{ij\alpha\beta}^{22*}}{2} + V_{ai}^\dagger U_{jb}^* J_{ij\alpha\beta}^{22*} \right) (f_\beta - f_\alpha) \chi_{\alpha\beta}^{22} \quad (\text{B.62})$$

$$+ \left(U_{ai}^\dagger V_{jb}^* K_{ij\alpha\beta}^{12} + U_{ai}^\dagger U_{jb}^* \frac{L_{ij\alpha\beta}^{12}}{2} - V_{ai}^\dagger V_{jb}^* \frac{L_{ij\alpha\beta}^{21*}}{2} + V_{ai}^\dagger U_{jb}^* K_{ij\alpha\beta}^{21*} \right) (1 - f_\alpha - f_\beta) \chi_{\alpha\beta}^{12} \quad (\text{B.63})$$

$$+ \left(U_{ai}^\dagger V_{jb}^* K_{ij\alpha\beta}^{21} + U_{ai}^\dagger U_{jb}^* \frac{L_{ij\alpha\beta}^{21}}{2} - V_{ai}^\dagger V_{jb}^* \frac{L_{ij\alpha\beta}^{12*}}{2} + V_{ai}^\dagger U_{jb}^* K_{ij\alpha\beta}^{12*} \right) (1 - f_\alpha - f_\beta) \chi_{\alpha\beta}^{21} \quad (\text{B.64})$$

$$\mathcal{H}_{(1),ab}^{21} = \left(V_{ai}^T U_{jb} J_{ij\alpha\beta}^{11} + V_{ai}^T V_{jb} \frac{M_{ij\alpha\beta}^{11}}{2} + U_{ai}^T U_{jb} \frac{M_{ij\alpha\beta}^{11*}}{2} + U_{ai}^T V_{jb} J_{ij\alpha\beta}^{11*} \right) (f_\beta - f_\alpha) \chi_{\alpha\beta}^{11} \quad (\text{B.65})$$

$$+ \left(V_{ai}^T U_{jb} J_{ij\alpha\beta}^{22} + V_{ai}^T V_{jb} \frac{M_{ij\alpha\beta}^{22}}{2} + U_{ai}^T U_{jb} \frac{M_{ij\alpha\beta}^{22*}}{2} + U_{ai}^T V_{jb} J_{ij\alpha\beta}^{22*} \right) (f_\beta - f_\alpha) \chi_{\alpha\beta}^{22} \quad (\text{B.66})$$

$$+ \left(V_{ai}^T U_{jb} K_{ij\alpha\beta}^{12} + V_{ai}^T V_{jb} \frac{L_{ij\alpha\beta}^{12}}{2} - U_{ai}^T U_{jb} \frac{L_{ij\alpha\beta}^{21*}}{2} + U_{ai}^T V_{jb} K_{ij\alpha\beta}^{21*} \right) (1 - f_\alpha - f_\beta) \chi_{\alpha\beta}^{12} \quad (\text{B.67})$$

$$+ \left(V_{ai}^T U_{jb} K_{ij\alpha\beta}^{21} + V_{ai}^T V_{jb} \frac{L_{ij\alpha\beta}^{21}}{2} - U_{ai}^T U_{jb} \frac{L_{ij\alpha\beta}^{12*}}{2} + U_{ai}^T V_{jb} K_{ij\alpha\beta}^{12*} \right) (1 - f_\alpha - f_\beta) \chi_{\alpha\beta}^{21} \quad (\text{B.68})$$

$$\mathcal{H}_{(1),ab}^{22} = \left(V_{ai}^T V_{jb}^* J_{ij\alpha\beta}^{11} + V_{ai}^T U_{jb}^* \frac{M_{ij\alpha\beta}^{11}}{2} + U_{ai}^T V_{jb}^* \frac{M_{ij\alpha\beta}^{11*}}{2} + U_{ai}^T U_{jb}^* J_{ij\alpha\beta}^{11*} \right) (f_\beta - f_\alpha) \chi_{\alpha\beta}^{11} \quad (\text{B.69})$$

$$+ \left(V_{ai}^T V_{jb}^* J_{ij\alpha\beta}^{22} + V_{ai}^T U_{jb}^* \frac{M_{ij\alpha\beta}^{22}}{2} + U_{ai}^T V_{jb}^* \frac{M_{ij\alpha\beta}^{22*}}{2} + U_{ai}^T U_{jb}^* J_{ij\alpha\beta}^{22*} \right) (f_\beta - f_\alpha) \chi_{\alpha\beta}^{22} \quad (\text{B.70})$$

$$+ \left(V_{ai}^T V_{jb}^* K_{ij\alpha\beta}^{12} + V_{ai}^T U_{jb}^* \frac{L_{ij\alpha\beta}^{12}}{2} - U_{ai}^T V_{jb}^* \frac{L_{ij\alpha\beta}^{21*}}{2} + U_{ai}^T U_{jb}^* K_{ij\alpha\beta}^{21*} \right) (1 - f_\alpha - f_\beta) \chi_{\alpha\beta}^{12} \quad (\text{B.71})$$

$$+ \left(V_{ai}^T V_{jb}^* K_{ij\alpha\beta}^{21} + V_{ai}^T U_{jb}^* \frac{L_{ij\alpha\beta}^{21}}{2} - U_{ai}^T V_{jb}^* \frac{L_{ij\alpha\beta}^{12*}}{2} + U_{ai}^T U_{jb}^* K_{ij\alpha\beta}^{12*} \right) (1 - f_\alpha - f_\beta) \chi_{\alpha\beta}^{21} \quad (\text{B.72})$$

Looking back to B.35, we see that we can write it in the same form as B.34:

$$\begin{aligned} \frac{1}{2} \text{Tr} (\mathcal{H}_1 \mathcal{R}_1) = & \bar{\mathcal{M}}''_{\alpha\beta ab}{}^{11,11} \chi_{\alpha\beta}^{11} \chi_{ba}^{11} + \bar{\mathcal{M}}''_{\alpha\beta ab}{}^{12,11} \chi_{\alpha\beta}^{12} \chi_{ba}^{11} + \bar{\mathcal{M}}''_{\alpha\beta ab}{}^{21,11} \chi_{\alpha\beta}^{21} \chi_{ba}^{11} + \bar{\mathcal{M}}''_{\alpha\beta ab}{}^{22,11} \chi_{\alpha\beta}^{22} \chi_{ba}^{11} \\ & \bar{\mathcal{M}}''_{\alpha\beta ab}{}^{11,12} \chi_{\alpha\beta}^{11} \chi_{ba}^{12} + \bar{\mathcal{M}}''_{\alpha\beta ab}{}^{12,12} \chi_{\alpha\beta}^{12} \chi_{ba}^{12} + \bar{\mathcal{M}}''_{\alpha\beta ab}{}^{21,12} \chi_{\alpha\beta}^{21} \chi_{ba}^{12} + \bar{\mathcal{M}}''_{\alpha\beta ab}{}^{22,12} \chi_{\alpha\beta}^{22} \chi_{ba}^{12} \\ & \bar{\mathcal{M}}''_{\alpha\beta ab}{}^{11,21} \chi_{\alpha\beta}^{11} \chi_{ba}^{21} + \bar{\mathcal{M}}''_{\alpha\beta ab}{}^{12,21} \chi_{\alpha\beta}^{12} \chi_{ba}^{21} + \bar{\mathcal{M}}''_{\alpha\beta ab}{}^{21,21} \chi_{\alpha\beta}^{21} \chi_{ba}^{21} + \bar{\mathcal{M}}''_{\alpha\beta ab}{}^{22,21} \chi_{\alpha\beta}^{22} \chi_{ba}^{21} \\ & \bar{\mathcal{M}}''_{\alpha\beta ab}{}^{11,22} \chi_{\alpha\beta}^{11} \chi_{ba}^{22} + \bar{\mathcal{M}}''_{\alpha\beta ab}{}^{12,22} \chi_{\alpha\beta}^{12} \chi_{ba}^{22} + \bar{\mathcal{M}}''_{\alpha\beta ab}{}^{21,22} \chi_{\alpha\beta}^{21} \chi_{ba}^{22} + \bar{\mathcal{M}}''_{\alpha\beta ab}{}^{22,22} \chi_{\alpha\beta}^{22} \chi_{ba}^{22} \end{aligned} \quad (\text{B.73})$$

B.3.4 Collective inertia tensor

B.3.4.1 The total kinetic energy

Expressions B.34 and B.73 can be combined into one single expression involving the vector-like object χ and the matrix-like object $\bar{\mathcal{M}} = 2(\bar{\mathcal{M}}' + \bar{\mathcal{M}}'')$

$$E_{kin} = \frac{1}{2} \chi^\dagger \bar{\mathcal{M}} \chi \quad (\text{B.74})$$

$$\chi_{\alpha\beta} \equiv \begin{pmatrix} \chi_{\alpha\beta}^{11} \\ \chi_{\alpha\beta}^{12} \\ \chi_{\alpha\beta}^{21} \\ \chi_{\alpha\beta}^{22} \end{pmatrix}, \quad \chi_{ab}^\dagger = \left(\chi_{ab}^{11*} \chi_{ab}^{12*} \chi_{ab}^{21*} \chi_{ab}^{22*} \right) \quad (\text{B.75})$$

$\bar{\mathcal{M}}$ is given by column in Table B.1.

Now we have an expression for the energy in terms of an inertia tensor $\bar{\mathcal{M}}$ and the expansion parameter χ . We already know that χ is related to time-dependent changes in the density $\dot{\mathcal{R}}_0$; now let us further try to relate χ to changes in the collective shape multipole moments of the nucleus \dot{q} .

Sanity Check: As in the case of the ATDHFB equations from Section B.3.2, in the $T = f = 0$ case, the 11 and 22 terms vanish completely in the lines leading up to B.34 and B.73 and we are left with familiar [zero-temperature] ATDHFB expressions. In essence, the rank of the problem reduces from dealing with a 4x4 matrix to dealing with a 2x2 matrix.

Table B.1: The full FT-ATDHFB matrix, listed by column

$$\begin{aligned}
& \bar{\mathcal{M}}_{1,1} = \frac{1}{2} \left(\begin{aligned} & (E_b - E_a)(f_a - f_b)\delta_{a\alpha}\delta_{b\beta} - (f_a - f_b) \left[\bar{v}_{ikjl} \left(U_{ai}^\dagger U_{jb} U_{l\alpha} U_{\beta k}^\dagger - V_{ai}^\dagger V_{jb} U_{l\alpha} U_{\beta k}^\dagger - V_{ai}^\dagger V_{jb} U_{l\alpha} V_{\beta k}^\dagger - V_{ai}^\dagger U_{jb} U_{l\alpha} V_{\beta k}^\dagger \right) + \frac{\bar{v}_{ijkl}}{2} \left(U_{ai}^\dagger V_{jb} U_{l\alpha} V_{\beta k}^\dagger - V_{ai}^\dagger U_{jb} U_{l\alpha} V_{\beta k}^\dagger \right) \right] (f_\beta - f_\alpha) \\ & (1 - f_a - f_b) \left[\bar{v}_{ikjl} \left(U_{ai}^\dagger V_{jb}^* U_{l\alpha} U_{\beta k}^\dagger - V_{ai}^\dagger U_{jb}^* U_{l\alpha} U_{\beta k}^\dagger \right) + \frac{\bar{v}_{ijkl}}{2} \left(U_{ai}^\dagger U_{jb}^* U_{l\alpha} V_{\beta k}^\dagger - V_{ai}^\dagger V_{jb}^* U_{l\alpha} V_{\beta k}^\dagger \right) \right] (f_\beta - f_\alpha) \\ & -(1 - f_a - f_b) \left[\bar{v}_{ikjl} \left(V_{ai}^T U_{jb} U_{l\alpha} U_{\beta k}^\dagger - U_{ai}^T V_{jb} U_{l\alpha} U_{\beta k}^\dagger \right) + \frac{\bar{v}_{ijkl}}{2} \left(V_{ai}^T V_{jb} U_{l\alpha} V_{\beta k}^\dagger - U_{ai}^T U_{jb} U_{l\alpha} V_{\beta k}^\dagger \right) \right] (f_\beta - f_\alpha) \\ & (f_a - f_b) \left[\bar{v}_{ikjl} \left(V_{ai}^T V_{jb}^* U_{l\alpha} U_{\beta k}^\dagger - U_{ai}^T U_{jb}^* U_{l\alpha} U_{\beta k}^\dagger \right) + \frac{\bar{v}_{ijkl}}{2} \left(V_{ai}^T U_{jb}^* U_{l\alpha} V_{\beta k}^\dagger - U_{ai}^T V_{jb}^* U_{l\alpha} V_{\beta k}^\dagger \right) \right] (f_\beta - f_\alpha) \end{aligned} \right] \quad (\text{B.76}) \\
& \bar{\mathcal{M}}_{1,2} = \frac{1}{2} \left(\begin{aligned} & -(f_a - f_b) \left[\bar{v}_{ikjl} \left(U_{ai}^\dagger U_{jb} U_{l\alpha} V_{\beta k}^T + V_{ai}^\dagger V_{jb} V_{l\alpha} U_{\beta k}^T \right) + \frac{\bar{v}_{ijkl}}{2} \left(U_{ai}^\dagger V_{jb} U_{l\alpha} U_{\beta k}^T - V_{ai}^\dagger U_{jb} V_{l\alpha} V_{\beta k}^T \right) \right] (1 - f_\alpha - f_\beta) \\ & (E_a + E_b)(1 - f_a - f_b)\delta_{a\alpha}\delta_{b\beta} + (1 - f_a - f_b) \left[\bar{v}_{ikjl} \left(U_{ai}^\dagger V_{jb}^* U_{l\alpha} V_{\beta k}^T + V_{ai}^\dagger U_{jb}^* U_{l\alpha} U_{\beta k}^T \right) + \frac{\bar{v}_{ijkl}}{2} \left(U_{ai}^\dagger U_{jb}^* U_{l\alpha} U_{\beta k}^T - V_{ai}^\dagger V_{jb}^* U_{l\alpha} V_{\beta k}^T \right) \right] \\ & -(1 - f_a - f_b) \left[\bar{v}_{ikjl} \left(V_{ai}^T U_{jb} U_{l\alpha} V_{\beta k}^T + U_{ai}^T V_{jb} V_{l\alpha} U_{\beta k}^T \right) + \frac{\bar{v}_{ijkl}}{2} \left(V_{ai}^T V_{jb} U_{l\alpha} U_{\beta k}^T - U_{ai}^T U_{jb} V_{l\alpha} V_{\beta k}^T \right) \right] (1 - f_\alpha - f_\beta) \\ & (f_a - f_b) \left[\bar{v}_{ikjl} \left(V_{ai}^T V_{jb}^* U_{l\alpha} V_{\beta k}^T + U_{ai}^T U_{jb}^* V_{l\alpha} U_{\beta k}^T \right) + \frac{\bar{v}_{ijkl}}{2} \left(V_{ai}^T U_{jb}^* U_{l\alpha} U_{\beta k}^T - U_{ai}^T V_{jb}^* V_{l\alpha} V_{\beta k}^T \right) \right] (1 - f_\alpha - f_\beta) \end{aligned} \right] \quad (\text{B.77}) \\
& \bar{\mathcal{M}}_{1,3} = \frac{1}{2} \left(\begin{aligned} & (f_a - f_b) \left[\bar{v}_{ikjl} \left(U_{ai}^\dagger U_{jb} V_{l\alpha}^* U_{\beta k}^\dagger + V_{ai}^\dagger V_{jb} U_{l\alpha}^* V_{\beta k}^\dagger \right) + \frac{\bar{v}_{ijkl}}{2} \left(U_{ai}^\dagger V_{jb} V_{l\alpha}^* U_{\beta k}^\dagger - V_{ai}^\dagger U_{jb} U_{l\alpha}^* V_{\beta k}^\dagger \right) \right] (1 - f_\alpha - f_\beta) \\ & -(1 - f_a - f_b) \left[\bar{v}_{ikjl} \left(U_{ai}^\dagger V_{jb}^* V_{l\alpha}^* U_{\beta k}^\dagger + V_{ai}^\dagger U_{jb}^* U_{l\alpha}^* V_{\beta k}^\dagger \right) + \frac{\bar{v}_{ijkl}}{2} \left(U_{ai}^\dagger U_{jb}^* V_{l\alpha}^* U_{\beta k}^\dagger - V_{ai}^\dagger V_{jb}^* U_{l\alpha}^* V_{\beta k}^\dagger \right) \right] (1 - f_\alpha - f_\beta) \\ & (E_a + E_b)(1 - f_a - f_b)\delta_{a\alpha}\delta_{b\beta} + (1 - f_a - f_b) \left[\bar{v}_{ikjl} \left(V_{ai}^T U_{jb} V_{l\alpha}^* U_{\beta k}^\dagger + U_{ai}^T V_{jb} U_{l\alpha}^* V_{\beta k}^\dagger \right) + \frac{\bar{v}_{ijkl}}{2} \left(V_{ai}^T V_{jb} V_{l\alpha}^* U_{\beta k}^\dagger - U_{ai}^T U_{jb} U_{l\alpha}^* V_{\beta k}^\dagger \right) \right] \\ & -(f_a - f_b) \left[\bar{v}_{ikjl} \left(V_{ai}^T V_{jb}^* V_{l\alpha}^* U_{\beta k}^\dagger + U_{ai}^T U_{jb}^* U_{l\alpha}^* V_{\beta k}^\dagger \right) + \frac{\bar{v}_{ijkl}}{2} \left(V_{ai}^T U_{jb}^* V_{l\alpha}^* U_{\beta k}^\dagger - U_{ai}^T V_{jb}^* U_{l\alpha}^* V_{\beta k}^\dagger \right) \right] (1 - f_\alpha - f_\beta) \end{aligned} \right] \quad (\text{B.78}) \\
& \bar{\mathcal{M}}_{1,4} = \frac{1}{2} \left(\begin{aligned} & (f_a - f_b) \left[\bar{v}_{ikjl} \left(U_{ai}^\dagger U_{jb} V_{l\alpha}^* V_{\beta k}^T - V_{ai}^\dagger V_{jb} V_{l\alpha} V_{\beta k}^T \right) + \frac{\bar{v}_{ijkl}}{2} \left(U_{ai}^\dagger V_{jb} V_{l\alpha}^* U_{\beta k}^T - V_{ai}^\dagger U_{jb} V_{l\alpha} U_{\beta k}^T \right) \right] + \left[(f_\beta - f_\alpha) \right. \\ & -(1 - f_a - f_b) \left[\bar{v}_{ikjl} \left(U_{ai}^\dagger V_{jb}^* V_{l\alpha}^* V_{\beta k}^T - V_{ai}^\dagger U_{jb}^* V_{l\alpha}^* V_{\beta k}^T \right) + \frac{\bar{v}_{ijkl}}{2} \left(U_{ai}^\dagger U_{jb}^* V_{l\alpha}^* U_{\beta k}^T - V_{ai}^\dagger V_{jb}^* V_{l\alpha}^* U_{\beta k}^T \right) \right] (f_\beta - f_\alpha) \\ & (1 - f_a - f_b) \left[\bar{v}_{ikjl} \left(V_{ai}^T U_{jb} V_{l\alpha}^* V_{\beta k}^T - U_{ai}^T V_{jb} V_{l\alpha}^* V_{\beta k}^T \right) + \frac{\bar{v}_{ijkl}}{2} \left(V_{ai}^T V_{jb} V_{l\alpha}^* U_{\beta k}^T - U_{ai}^T U_{jb} V_{l\alpha}^* U_{\beta k}^T \right) \right] (f_\beta - f_\alpha) \\ & (E_b - E_a)(f_a - f_b)\delta_{a\alpha}\delta_{b\beta} - (f_a - f_b) \left[\bar{v}_{ikjl} \left(V_{ai}^T V_{jb}^* V_{l\alpha}^* V_{\beta k}^T - U_{ai}^T U_{jb}^* V_{l\alpha}^* V_{\beta k}^T \right) + \frac{\bar{v}_{ijkl}}{2} \left(V_{ai}^T U_{jb}^* V_{l\alpha}^* U_{\beta k}^T - U_{ai}^T V_{jb}^* V_{l\alpha}^* U_{\beta k}^T \right) \right] (f_\beta - f_\alpha) \end{aligned} \right] \quad (\text{B.79})
\end{aligned}$$

B.3.4.2 Cranking approximation

We already introduced the cranking approximation briefly in Section B.3.2 to simplify the relation between χ and $\dot{\mathcal{R}}_0$ when we assumed that changes in the density will have approximately no effect on the mean field ($\mathcal{H}_1 \approx 0$). We can apply this to the energy expression, and then the inertia tensor is much simpler:

$$\bar{\mathcal{M}} = \frac{1}{4} \begin{pmatrix} (E_b - E_a)(f_a - f_b) & 0 & 0 & 0 \\ 0 & (E_a + E_b)(1 - f_a - f_b) & 0 & 0 \\ 0 & 0 & (E_a + E_b)(1 - f_a - f_b) & 0 \\ 0 & 0 & 0 & (E_b - E_a)(f_a - f_b) \end{pmatrix} \quad (\text{B.80})$$

B.3.4.3 Collective shape space

Suppose there is a set of collective variables (q_1, q_2, \dots, q_n) which describe changes in the density $\mathcal{R}_0(t)$ at all times t . Then

$$\dot{\mathcal{R}}_0 = \sum_{\mu=1}^n \dot{q}_\mu \frac{\partial \mathcal{R}_0}{\partial q_\mu} \quad (\text{B.81})$$

Relating this back to χ using equations B.20 (we'll just stick with the cranking approximation here) gives

$$\chi_{ab}^{11} = \sum_{\mu=1}^n \frac{\hbar \dot{q}_{\mu}}{(E_a - E_b)(f_b - f_a)} \frac{\partial \mathcal{R}_{(0),ab}^{11}}{\partial q_{\mu}} \quad (\text{B.82})$$

$$\chi_{ab}^{12} = \sum_{\mu=1}^n \frac{\hbar \dot{q}_{\mu}}{(E_a + E_b)(1 - f_a - f_b)} \frac{\partial \mathcal{R}_{(0),ab}^{12}}{\partial q_{\mu}} \quad (\text{B.83})$$

$$\chi_{ab}^{21} = \sum_{\mu=1}^n \frac{\hbar \dot{q}_{\mu}}{(E_a + E_b)(1 - f_a - f_b)} \frac{\partial \mathcal{R}_{(0),ab}^{21}}{\partial q_{\mu}} \quad (\text{B.84})$$

$$\chi_{ab}^{22} = \sum_{\mu=1}^n \frac{\hbar \dot{q}_{\mu}}{(E_a - E_b)(f_b - f_a)} \frac{\partial \mathcal{R}_{(0),ab}^{22}}{\partial q_{\mu}} \quad (\text{B.85})$$

$$(\text{B.86})$$

Of course, we should be careful here if the temperature is allowed to approach zero. In that case, then from equation B.20 we see that $\dot{\mathcal{R}}^{11} = \dot{\mathcal{R}}^{22} = 0$. We should not have any χ^{11} or χ^{22} terms in the zero temperature case. The final form of the inertia tensor will also be affected. Likewise we should be careful not to divide by zero in the case of $E_a = E_b$ as mentioned earlier at the end of Section B.3.2.

If we take this now and plug it into our energy expression B.74 using the cranked inertia tensor B.80, the result is the following:

$$E_{kin} \approx \frac{1}{2} \sum_{\mu\nu} \dot{q}_{\mu} \dot{q}_{\nu} \mathbf{M}_{\mu\nu} \quad (\text{B.87})$$

where

$$\begin{aligned}
M_{\mu\nu} = \frac{\hbar^2}{2} & \left[\frac{1}{(E_a - E_b)(f_b - f_a)} \left(\frac{\partial \mathcal{R}_{(0),ab}^{11}}{\partial q_\mu} \frac{\partial \mathcal{R}_{(0),ba}^{11}}{\partial q_\nu} + \frac{\partial \mathcal{R}_{(0),ab}^{22}}{\partial q_\mu} \frac{\partial \mathcal{R}_{(0),ba}^{22}}{\partial q_\mu} \right) + \right. \\
& \left. \frac{1}{(E_a + E_b)(1 - f_a - f_b)} \left(\frac{\partial \mathcal{R}_{(0),ab}^{21}}{\partial q_\mu} \frac{\partial \mathcal{R}_{(0),ba}^{12}}{\partial q_\nu} + \frac{\partial \mathcal{R}_{(0),ab}^{12}}{\partial q_\mu} \frac{\partial \mathcal{R}_{(0),ba}^{21}}{\partial q_\mu} \right) \right]
\end{aligned}
\tag{B.88}$$

In the zero temperature case, the first piece (involving \mathcal{R}^{11} and \mathcal{R}^{22}) should be replaced with zero.

B.4 Numerical implementation

Numerical implementations of the FT-ATDHFB inertia may encounter some challenges. First, as discussed in Section 3.2 we know there is an ideal range of values δq to use when computing derivatives of \mathcal{R} using finite differences. Too large, and the derivative is artificially-smoothed out; too small, and densities of adjacent points can become indistinguishable (dependent on the HFB convergence parameter). Additionally, there may be problems when dealing with small, non-zero temperatures (or, more generally, when $f_b - f_a$ is small).

We might consider introducing a cutoff on the difference $f_b - f_a$. If we make our cutoff too tight, we start cutting off physics (the tail of the Fermi distribution). If we leave our cutoff too small, we start dividing by numbers that are smaller than the noise in the density matrix which will lead to the inertia blowing up.

As an example, suppose we take a value $\delta q = 10^{-3}$ and set our HFB convergence parameter to 10^{-7} . Roughly-speaking, then, we would expect that we can set a cutoff for $f_b - f_a$

of something around 10^{-4} or so and still obtain reasonable results.

This was done for a ^{240}Pu calculation with a few different cutoff values. First the exact $T=0$ inertia was computed. Then the inertia was computed again using the same densities which had been computed at $T=0$, but introducing a fake temperature $T=0.05$ to calculate the inertia. The results, shown in the following table, indicate the presence of an ideal cutoff parameter that is in the neighborhood of our prediction:

| Convergence | 10^{-7} | |
|-----------------------|----------------|----------------|
| δq | 10^{-3} | |
| Actual $T=0$ inertia: | 1.585632E-02 | |
| Cutoff | Inertia | % error |
| 10^{-4} | 1.585205E-02 | -2.692933E-04 |
| 10^{-5} | 1.585622E-02 | -6.306634E-06 |
| 10^{-6} | 1.585697E-02 | 4.099312E-05 |
| 10^{-7} | 1.587771E-02 | 1.348989E-03 |
| 10^{-8} | 1.612200E-02 | 1.675546E-02 |

Appendix C

List of My Contributions

- **Observation of the competing fission modes in ^{178}Pt**
 - *Phys. Lett. B* 790, 583-588 (2019)
 - Performed PES calculations
 - Created graphics for Figure 3
 - Suggested several revisions to the text of the article
- **Colloquium: Superheavy elements: Oganesson and beyond**
 - *Rev. Mod. Phys.* 91, 011001 (2019)
 - Generated Figure 12
 - Helped write Section VI: Fission
 - Suggested comments and revisions to the text
- **Cluster radioactivity of ^{294}Og**
 - ???
 - Lead author on paper/wrote first draft
 - Did all UNEDF1_{HFB} calculations and SkM* Langevin calculations
 - Generated all figures

- **Microscopic Calculation of Fission Mass Distributions at Increasing Excitation Energies**

- *CNR2018 Proceedings...*
- Helped derive [one of the equations]
- Contributed to discussion of ???

- **Fission Tools**

- *Suite of codes which extend the functionality of HFODD, HFBTHO, and other DFT solvers to the problem of nuclear fission.*
- https://gitlab.com/zachmath/fission_tools
- Maintainer, 47 commits
- Converted old codes from Fortran77 to Fortran90
- Implemented shared memory (OpenMP) and distributed memory (MPI) parallelism
- Improved documentation, flexibility, and user-friendliness
- Created several Python-based utilities for plotting and file handling
- Increased functionality, such as by increasing from 2D to 3D or 4D

- **PES Tools**

- *Python framework for handling potential energy surfaces as XML files*
- https://gitlab.com/schuncknf/pes_tools
- Developer, 24 commits

- Added a `point` class with various methods to use on a single point of a PES
- Interface to `fission_tools`
- Various updates bugfixes

- **DFTNESS**

- *DFTNESS (Density Functional Theory for Nuclei at Extreme ScaleS) is a computational framework to solve the equation of nuclear density functional theory. It is based on the two solvers HFBTHO and HFODD.*
- <https://gitlab.com/schuncknf/dftness>
- <https://gitlab.com/schuncknf/dftness>
- Developer, 60 commits
- OpenMP parallelization of subroutine `QMULCM`
- Various updates and bugfixes
- Most of these commits were related to `fission_tools`, before that was all moved to a separate repository

BIBLIOGRAPHY

- [1] O. Hahn and F. Strassmann, *Naturwissenschaften* **27**, 11 (1939).
- [2] L. Meitner and O. R. Frisch, *Nature* **143**, 239 (1939).
- [3] N. Bohr, *Nature* **143**, 330 (1939).
- [4] G. Flerov and K. Petrjak, *Phys. Rev.* **58**, 89 (1940).
- [5] C. F. v. Weizsäcker, *Zeitschrift für Phys.* **96**, 431 (1935).
- [6] N. Bohr and J. A. Wheeler, *Phys. Rev.* **56**, 426 (1939).
- [7] S. M. Polikanov, V. A. Druin, V. A. Karnaukhov, V. L. Mikheev, A. A. Pleve, N. K. Skobelev, V. G. Subbotin, G. M. Terakopyan, and V. A. Fomichev, *Sov. Physics JETP-USSR* **15**, 1016 (1962).
- [8] S. G. Nilsson, *Mat. Fys. Medd. Dan. Vid. Selsk.* **16** (1955).
- [9] V. Strutinsky, *Nucl. Phys. A* **95**, 420 (1967).
- [10] V. Strutinsky, *Nucl. Phys. A* **122**, 1 (1968).
- [11] M. Brack, J. Damgaard, A. S. Jensen, H. C. Pauli, V. M. Strutinsky, and C. Y. Wong, *Rev. Mod. Phys.* **44**, 320 (1972).
- [12] P. Möller and J. Randrup, *Phys. Rev. C* **91**, 44316 (2015).
- [13] P. Möller, A. J. Sierk, T. Ichikawa, A. Iwamoto, and M. Mumpower, *Phys. Rev. C* **91**, 24310 (2015).
- [14] P. Jachimowicz, M. Kowal, and J. Skalski, *Phys. Rev. C* **87**, 044308 (2013).
- [15] P. Jachimowicz, M. Kowal, and J. Skalski, *Phys. Rev. C* **95**, 14303 (2017).
- [16] J. Carlson, M. J. Savage, R. Gerber, K. Antypas, D. Bard, R. Coffey, E. Dart, S. Dosanjh, J. Hack, I. Monga, M. E. Papka, K. Riley, L. Rotman, T. Straatsma, J. Wells, H. Avakian, Y. Ayyad, S. A. Bass, D. Bazin, A. Boehnlein, G. Bollen, L. J. Broussard, A. Calder, S. Couch, A. Couture, M. Cromaz, W. Detmold, J. Detwiler, H. Duan, R. Edwards, J. Engel, C. Fryer, G. M. Fuller, S. Gandolfi, G. Gavalian, D. Georgobiani, R. Gupta, V. Gyurjyan, M. Hausmann, G. Heyes, W. R. Hix, M. Ito,

- G. Jansen, R. Jones, B. Joo, O. Kaczmarek, D. Kasen, M. Kostin, T. Kurth, J. Lauret, D. Lawrence, H.-W. Lin, M. Lin, P. Mantica, P. Maris, B. Messer, W. Mittig, S. Mosby, S. Mukherjee, H. A. Nam, P. Navratil, W. Nazarewicz, E. Ng, T. O'Donnell, K. Orginos, F. Pellemoine, P. Petreczky, S. C. Pieper, C. H. Pinkenburg, B. Plaster, R. J. Porter, M. Portillo, S. Pratt, M. L. Purschke, J. Qiang, S. Quaglioni, D. Richards, Y. Roblin, B. Schenke, R. Schiavilla, S. Schlichting, N. Schunck, P. Steinbrecher, M. Strickland, S. Syritsyn, B. Terzic, R. Varner, J. Vary, S. Wild, F. Winter, R. Zegers, H. Zhang, V. Ziegler, and M. Zingale, (2017), 10.2172/1369223.
- [17] N. Schunck and L. M. Robledo, Reports Prog. Phys. **79**, 116301 (2016).
 - [18] T. Baumann, M. Hausmann, B. Sherrill, and O. Tarasov, Nucl. Instruments Methods Phys. Res. Sect. B Beam Interact. with Mater. Atoms **376**, 33 (2016).
 - [19] G. Scamps and C. Simenel, (2018), arXiv:1804.03337 .
 - [20] G. Scamps, C. Simenel, and D. Lacroix, AIP Conf. Proc. **1681**, 040003 (2015).
 - [21] C. Simenel and A. S. Umar, Phys. Rev. C **89**, 031601 (2014).
 - [22] J. Grineviciute, P. Magierski, A. Bulgac, S. Jin, and I. Stetcu, Acta Phys. Pol. B **49**, 591 (2018).
 - [23] A. S. Umar, V. E. Oberacker, J. A. Maruhn, and P.-G. Reinhard, J. Phys. G Nucl. Part. Phys. **37**, 064037 (2010).
 - [24] G. Scamps, C. Simenel, and D. Lacroix, Phys. Rev. C **92**, 011602 (2015).
 - [25] A. Bulgac, S. Jin, K. Roche, N. Schunck, and I. Stetcu, (2018), arXiv:1806.00694 .
 - [26] D. Jacquet and M. Morjean, Prog. Part. Nucl. Phys. **63**, 155 (2009).
 - [27] W. Nazarewicz, Nucl. Phys. A **557**, 489 (1993).
 - [28] W. Younes and D. Gogny, Phys. Rev. Lett. **107**, 132501 (2011), arXiv:1103.3466 .
 - [29] P. Hohenberg and W. Kohn, Phys. Rev. **136**, B864 (1964).
 - [30] W. Kohn and L. J. Sham, Phys. Rev. **140**, A1133 (1965).
 - [31] J. C. Slater, Phys. Rev. **81**, 385 (1951).
 - [32] C. Titin-Schnaider and P. Quentin, Phys. Lett. B **49**, 397 (1974).
 - [33] R. Machleidt and D. Entem, Phys. Rep. **503**, 1 (2011).
 - [34] R. Machleidt and F. Sammarruca, Phys. Scr. **91**, 083007 (2016).
 - [35] E. Epelbaum, H.-W. Hammer, and U.-G. Meißner, Rev. Mod. Phys. **81**, 1773 (2009).

- [36] W. Detmold, “Nuclear physics from lattice qcd,” in *Lattice QCD Nucl. Phys.*, edited by H.-W. Lin and H. B. Meyer (Springer International Publishing, Cham, 2015) pp. 153–194.
- [37] S. R. Stroberg, S. K. Bogner, H. Hergert, and J. D. Holt, (2019), arXiv:1902.06154 .
- [38] M. Bender, P.-H. Heenen, and P.-G. Reinhard, *Rev. Mod. Phys.* **75**, 121 (2003), arXiv:9910025 [nucl-th] .
- [39] J. Bartel, P. Quentin, M. Brack, C. Guet, and H.-B. Håkansson, *Nucl. Phys. A* **386**, 79 (1982).
- [40] M. Kortelainen, J. McDonnell, W. Nazarewicz, P.-G. Reinhard, J. Sarich, N. Schunck, M. V. Stoitsov, and S. M. Wild, *Phys. Rev. C* **85**, 024304 (2012), arXiv:arXiv:1111.4344v2 .
- [41] N. Schunck, J. D. McDonnell, J. Sarich, S. M. Wild, and D. Higdon, *J. Phys. G Nucl. Part. Phys.* **42**, 034024 (2015).
- [42] P. Ring and P. Schuck, *The Nuclear Many-Body Problem*, edited by W. Beiglbock, M. Goldhaber, E. H. Lieb, and W. Thirring (Springer-Verlag, New York, 1980) p. 716.
- [43] C. L. Zhang, B. Schuetrumpf, and W. Nazarewicz, *Phys. Rev. C* **94**, 064323 (2016), arXiv:arXiv:1607.00422v3 .
- [44] J. Sadhukhan, C. Zhang, W. Nazarewicz, and N. Schunck, *Phys. Rev. C* **96**, 061301 (2017), arXiv:1711.10681 .
- [45] J. Sadhukhan, W. Nazarewicz, and N. Schunck, *Phys. Rev. C* **93**, 011304 (2016), arXiv:1510.08003 .
- [46] J. Sadhukhan, K. Mazurek, A. Baran, J. Dobaczewski, W. Nazarewicz, and J. A. Sheikh, *Phys. Rev. C* **88**, 064314 (2013), arXiv:1310.2003 .
- [47] A. Baran, J. A. Sheikh, J. Dobaczewski, W. Nazarewicz, and A. Staszczak, *Phys. Rev. C* **84**, 054321 (2011), arXiv:1007.3763 .
- [48] S. A. Giuliani and L. M. Robledo, *Phys. Lett. B* **787**, 134 (2018).
- [49] A. Baran, K. Pomorski, A. Lukasiak, and A. Sobieczewski, *Nucl. Phys. A* **361**, 83 (1981).
- [50] A. Baran, *Phys. Lett. B* **76**, 8 (1978).
- [51] K.-H. Schmidt and B. Jurado, *Reports Prog. Phys.* **81**, 106301 (2018), arXiv:1804.10421 .
- [52] N. Schunck, J. Dobaczewski, W. Satuła, P. Baczyk, J. Dudek, Y. Gao, M. Konieczka, K. Sato, Y. Shi, X. Wang, and T. Werner, *Comput. Phys. Commun.* **216**, 145 (2017), arXiv:1612.05314 .

- [53] R. N. Perez, N. Schunck, R.-D. Lasserri, C. Zhang, and J. Sarich, *Comput. Phys. Commun.* **220**, 363 (2017), arXiv:0406075 [nucl-th] .
- [54] N. Schunck, Z. Matheson, and E. Ney, “Pes tools,” (2019).
- [55] J. Sadhukhan, Z. Matheson, and S. A. Giuliani, “Fission tools,” (2019).
- [56] A. N. Andreyev, J. Elseviers, M. Huyse, P. Van Duppen, S. Antalic, A. Barzakh, N. Bree, T. E. Cocolios, V. F. Comas, J. Diriken, D. Fedorov, V. Fedosseev, S. Franchoo, J. A. Heredia, O. Ivanov, U. Köster, B. A. Marsh, K. Nishio, R. D. Page, N. Patronis, M. Seliverstov, I. Tsekhanovich, P. Van den Bergh, J. Van De Walle, M. Venhart, S. Vermote, M. Veselsky, C. Wagemans, T. Ichikawa, A. Iwamoto, P. Möller, and A. J. Sierk, *Phys. Rev. Lett.* **105**, 252502 (2010).
- [57] M. Warda and J. L. Egido, *Phys. Rev. C* **86**, 014322 (2012), arXiv:1204.5867 .
- [58] P. Möller, J. Randrup, and A. J. Sierk, *Phys. Rev. C* **85**, 024306 (2012).
- [59] J. D. McDonnell, W. Nazarewicz, J. A. Sheikh, A. Staszczak, and M. Warda, *Phys. Rev. C* **90**, 021302 (2014), arXiv:arXiv:1406.6955v1 .
- [60] T. Ichikawa and P. Möller, *Phys. Lett. B* **789**, 679 (2019).
- [61] V. Liberati, A. N. Andreyev, S. Antalic, A. Barzakh, T. E. Cocolios, J. Elseviers, D. Fedorov, V. N. Fedoseev, M. Huyse, D. T. Joss, Z. Kalaninová, U. Köster, J. F. W. Lane, B. Marsh, D. Mengoni, P. Molkanov, K. Nishio, R. D. Page, N. Patronis, D. Pauwels, D. Radulov, M. Seliverstov, M. Sjödin, I. Tsekhanovich, P. Van den Bergh, P. Van Duppen, M. Venhart, and M. Veselský, *Phys. Rev. C* **88**, 044322 (2013).
- [62] A. N. Andreyev, K. Nishio, and K.-H. Schmidt, *Reports Prog. Phys.* **81**, 016301 (2018).
- [63] I. Tsekhanovich, A. Andreyev, K. Nishio, D. Denis-Petit, K. Hirose, H. Makii, Z. Matheson, K. Morimoto, K. Morita, W. Nazarewicz, R. Orlandi, J. Sadhukhan, T. Tanaka, M. Vermeulen, and M. Warda, *Phys. Lett. B* **790**, 583 (2019), arXiv:1804.01832 .
- [64] J. Berger, M. Girod, and D. Gogny, *Nucl. Phys. A* **502**, 85 (1989).
- [65] T. Ichikawa, A. Iwamoto, P. Möller, and A. J. Sierk, *Phys. Rev. C* **86**, 24610 (2012).
- [66] M. Warda, A. Staszczak, and W. Nazarewicz, *Phys. Rev. C* **86**, 024601 (2012), arXiv:arXiv:1205.5797v2 .
- [67] G. Scamps and C. Simenel, *Nature* **564**, 382 (2018), arXiv:arXiv:1804.03337v2 .
- [68] A. V. Karpov, V. I. Zagrebaev, Y. M. Palenzuela, and W. Greiner, , 1.
- [69] D. N. Poenaru, R. A. Gherghescu, and W. Greiner, *Phys. Rev. Lett.* **107**, 062503 (2011).

- [70] D. N. Poenaru, R. A. Gherghescu, and W. Greiner, *Phys. Rev. C* **85**, 034615 (2012).
- [71] D. N. Poenaru, R. A. Gherghescu, and W. Greiner, *J. Phys. Conf. Ser.* **436**, 012056 (2013).
- [72] D. N. Poenaru, R. A. Gherghescu, W. Greiner, and N. S. Shakib, “How rare is cluster decay of superheavy nuclei?” in *Nucl. Phys. Present Futur.* (Springer International Publishing, Cham, 2015) pp. 131–140.
- [73] D. N. Poenaru and R. A. Gherghescu, *Phys. Rev. C* **97**, 044621 (2018).
- [74] K. P. Santhosh and C. Nithya, *Phys. Rev. C* **97**, 064616 (2018).
- [75] Y. L. Zhang and Y. Z. Wang, *Phys. Rev. C* **97**, 014318 (2018).
- [76] M. Warda, A. Zdeb, and L. M. Robledo, *Phys. Rev. C* **98**, 041602 (2018).
- [77] A. Sandulescu, D. Poenaru, and W. Greiner, *Sov. J. Part. Nucl.* **11**, 528 (1980).
- [78] D. Poenaru, W. Greiner, K. Depta, M. Ivascu, D. Mazilu, and A. Sandulescu, *At. Data Nucl. Data Tables* **34**, 423 (1986).
- [79] G. Royer, R. K. Gupta, and V. Denisov, *Nucl. Phys. A* **632**, 275 (1998).
- [80] D. N. Poenaru and W. Greiner, “Cluster radioactivity,” in *Clust. Nucl. Vol. 1*, edited by C. Beck (Springer Berlin Heidelberg, Berlin, Heidelberg, 2010) pp. 1–56.
- [81] M. Warda and L. M. Robledo, *Phys. Rev. C* **84**, 044608 (2011), arXiv:1107.1478 .
- [82] H. J. Rose and G. A. Jones, *Nature* **307**, 245 (1984).
- [83] A. Staszczak, A. Baran, and W. Nazarewicz, *Phys. Rev. C* **87**, 024320 (2013), arXiv:arXiv:1208.1215v1 .
- [84] A. Baran, M. Kowal, P.-G. Reinhard, L. M. Robledo, A. Staszczak, and M. Warda, *Nucl. Phys. A* **944**, 442 (2015), arXiv:1503.01608 .
- [85] N. T. Brewer, V. K. Utyonkov, K. P. Rykaczewski, Y. T. Oganessian, F. S. Abdullin, R. A. Boll, D. J. Dean, S. N. Dmitriev, J. G. Ezold, L. K. Felker, R. K. Grzywacz, M. G. Itkis, N. D. Kovrizhnykh, D. C. McInturff, K. Miernik, G. D. Owen, A. N. Polyakov, A. G. Popeko, J. B. Roberto, A. V. Sabel’nikov, R. N. Sagaidak, I. V. Shirokovsky, M. V. Shumeiko, N. J. Sims, E. H. Smith, V. G. Subbotin, A. M. Sukhov, A. I. Svirikhin, Y. S. Tsyganov, S. M. Van Cleve, A. A. Voinov, G. K. Vostokin, C. S. White, J. H. Hamilton, and M. A. Stoyer, *Phys. Rev. C* **98**, 024317 (2018).
- [86] S. A. Giuliani, L. M. Robledo, and R. Rodríguez-Guzmán, *Phys. Rev. C* **90**, 054311 (2014).
- [87] J. Sadhukhan, J. Dobaczewski, W. Nazarewicz, J. A. Sheikh, and A. Baran, *Phys. Rev. C* **90**, 061304 (2014), arXiv:arXiv:1410.1264v1 .

- [88] P.-H. Heenen, J. Skalski, A. Staszczak, and D. Vretenar, Nucl. Phys. A **944**, 415 (2015).
- [89] S. A. Giuliani, Z. Matheson, W. Nazarewicz, E. Olsen, P.-G. Reinhard, J. Sadhukhan, B. Schuetrumpf, N. Schunck, and P. Schwerdtfeger, Rev. Mod. Phys. **91**, 011001 (2019).
- [90] NNDC, “Interactive chart of nuclides, nudat 2.7,” (2018).
- [91] J. Randrup, P. Möller, and A. J. Sierk, Phys. Rev. C **84**, 034613 (2011).
- [92] A. J. Sierk, Phys. Rev. C **96**, 034603 (2017), arXiv:1711.02234 .
- [93] Y. T. Oganessian, V. K. Utyonkov, Y. V. Lobanov, F. S. Abdullin, A. N. Polyakov, R. N. Sagaidak, I. V. Shirokovsky, Y. S. Tsyganov, A. A. Voinov, G. G. Gulbekian, S. L. Bogomolov, B. N. Gikal, A. N. Mezentsev, S. Iliev, V. G. Subbotin, A. M. Sukhov, K. Subotic, V. I. Zagrebaev, G. K. Vostokin, M. G. Itkis, K. J. Moody, J. B. Patin, D. A. Shaughnessy, M. A. Stoyer, N. J. Stoyer, P. A. Wilk, J. M. Kenneally, J. H. Landrum, J. F. Wild, and R. W. Loughheed, Phys. Rev. C **74**, 044602 (2006).
- [94] Y. Oganessian, V. Utyonkov, Y. Lobanov, F. Abdullin, A. Polyakov, I. Shirokovsky, Y. Tsyganov, G. Gulbekian, S. Bogomolov, B. Gikal, A. Mezentsev, S. Iliev, V. Subbotin, A. Sukhov, A. Voinov, G. Buklanov, K. Subotic, V. Zagrebaev, M. Itkis, J. Patin, K. Moody, J. Wild, M. Stoyer, N. Stoyer, D. Shaughnessy, J. Kenneally, and R. Loughheed, Nucl. Phys. A **734**, 109 (2004).
- [95] M. Arnould, S. Goriely, and K. Takahashi, Phys. Rep. **450**, 97 (2007).
- [96] J. Beun, G. C. McLaughlin, R. Surman, and W. R. Hix, Phys. Rev. C **77**, 035804 (2008).
- [97] S. Goriely, Eur. Phys. J. A **51**, 22 (2015).
- [98] M. Eichler, A. Arcones, A. Kelic, O. Korobkin, K. Langanke, T. Marketin, G. Martinez-Pinedo, I. Panov, T. Rauscher, S. Rosswog, C. Winteler, N. T. Zinner, and F.-K. Thielemann, Astrophys. J. **808**, 30 (2015).
- [99] N. Schunck, D. Duke, H. Carr, and A. Knoll, Phys. Rev. C **90**, 054305 (2014), arXiv:1311.2616 .
- [100] N. Schunck, D. Duke, and H. Carr, Phys. Rev. C **91**, 034327 (2015), arXiv:1311.2620 .
- [101] E. Pian, P. D’Avanzo, S. Benetti, M. Branchesi, E. Brocato, S. Campana, E. Cappellaro, S. Covino, V. D’Elia, J. P. U. Fynbo, F. Getman, G. Ghirlanda, G. Ghisellini, A. Grado, G. Greco, J. Hjorth, C. Kouveliotou, A. Levan, L. Limatola, D. Malesani, P. A. Mazzali, A. Melandri, P. Møller, L. Nicastro, E. Palazzi, S. Piranomonte, A. Rossi, O. S. Salafia, J. Selsing, G. Stratta, M. Tanaka, N. R. Tanvir, L. Tomasella, D. Watson, S. Yang, L. Amati, L. A. Antonelli, S. Ascenzi, M. G. Bernardini, M. Boër,

- F. Bufano, A. Bulgarelli, M. Capaccioli, P. Casella, A. J. Castro-Tirado, E. Chassande-Mottin, R. Cioffi, C. M. Copperwheat, M. Dadina, G. De Cesare, A. Di Paola, Y. Z. Fan, B. Gendre, G. Giuffrida, A. Giunta, L. K. Hunt, G. L. Israel, Z.-P. Jin, M. M. Kasliwal, S. Klose, M. Lisi, F. Longo, E. Maiorano, M. Mapelli, N. Masetti, L. Nava, B. Patricelli, D. Perley, A. Pescalli, T. Piran, A. Possenti, L. Pulone, M. Razzano, R. Salvaterra, P. Schipani, M. Spera, A. Stamerra, L. Stella, G. Tagliaferri, V. Testa, E. Troja, M. Turatto, S. D. Vergani, and D. Vergani, *Nature* **551**, 67 (2017).
- [102] D. Kasen, B. Metzger, J. Barnes, E. Quataert, and E. Ramirez-Ruiz, *Nature* **551**, 80 (2017).
- [103] K. Nakamura, T. Kajino, G. J. Mathews, S. Sato, and S. Harikae, *Int. J. Mod. Phys. E* **22**, 1330022 (2013).
- [104] D. M. Siegel, J. Barnes, and B. D. Metzger, (2018), arXiv:1810.00098 .
- [105] Y. Zhu, R. T. Wollaeger, N. Vassh, R. Surman, T. M. Sprouse, M. R. Mumpower, P. Möller, G. C. McLaughlin, O. Korobkin, T. Kawano, P. J. Jaffke, E. M. Holmbeck, C. L. Fryer, W. P. Even, A. J. Couture, and J. Barnes, *Astrophys. J.* **863**, L23 (2018).
- [106] R. Brandt, S. G. Thompson, R. C. Gatti, and L. Phillips, *Phys. Rev.* **131**, 2617 (1963).
- [107] W. Younes and D. Gogny, *Phys. Rev. C* **80**, 054313 (2009), arXiv:0910.1284 .
- [108] A. L. Goodman, *Nucl. Phys. A* **352**, 30 (1981).
- [109] M. Baranger and M. Vénéroni, *Ann. Phys. (N. Y.)*. **114**, 123 (1978).